SAND2004-2869
Printed June 2004

Nanosecond Electrical Explosion of Thin Aluminum Wire in Vacuum: Experimental and Computational Investigations

G. S. Sarkisov[1*], S. E. Rosenthal, K. R. Cochrane[1], K. W. Struve,
C. Deeney, and D. H. McDaniel
Sandia National Laboratories, Albuquerque, NM 87185, USA
[1]Ktech Corporation, Albuquerque, NM 87123, USA

The experimental and computational investigations of nanosecond electrical explosion of thin Al wire in vacuum are presented. We have demonstrated that increasing the current rate leads to increased energy deposited before voltage collapse. Laser shadowgrams of the overheated Al core exhibit axial stratification with a ~100μm period. The experimental evidence for synchronization of the wire expansion and light emission with voltage collapse is presented. Two-wavelength interferometry shows an expanding Al core in a low-ionized gas condition with increasing ionization toward the periphery. Hydrocarbons are indicated in optical spectra and their influence on breakdown physics is discussed. The radial velocity of low-density plasma reaches a value of ~100 km/s. The possibility of an overcritical phase transition due to high pressure is discussed. 1D MHD simulation shows good agreement with experimental data. MHD simulation demonstrates separation of the exploding wire into a high-density cold core and a low-density hot corona as well as fast rejection of the current from the wire core to the corona during voltage collapse. Important features of the dynamics for wire core and corona follow from the MHD simulation and are discussed.

PACS numbers: 52.80.Qj, 52.70.Kz, 52.65.Kj

[*]e-mail: *gssarki@sandia.gov*

1. INTRODUCTION

The initial stage of the electrical explosion of fine metal wires is very important for modern z-pinch physics. The impressive result [1,2] achieved on the Z-facility at Sandia National Laboratories, of 1.8 MJ of x-rays radiated in 5 ns FWHM, gives great motivation for wire initiation research. Understanding wire initiation physics can lead to more realistic models used in numerical simulation of multi-wire array implosion, thereby allowing simulations to consistently predict final plasma stagnation and x-ray burst starting from cold wires. Investigation of wire initiation is also important because the initiation process can affect the symmetry of plasma stagnation and x-ray yield. The early advances in exploding wire science were summarized in two review papers [4,5]. The latest experiments on imploding Al wire arrays at Imperial College [3] show that wire initiation during prepulse exerts a strong influence on final x-ray yield.

Explosion of Al wire with a current rate of 3-10 A/ns results in voltage collapse in ~50 ns and core expansion with a velocity of ~1 km/s [6]. At this current rate the deposited energy into Al wire is nearly half the vaporization energy and the core exhibits a “foam-like” structure with ~10 μm spatial scale. The MHD simulation of exploding Al wire for extremely fast rising current through the wire ~1000 A/ns has been reported in [7]. This current rise for a single wire is ~30 times faster than during prepulse on the Z machine, and the results are not generally applicable to the Z case. For example, the total Al wire vaporization in [7] occurs during ~1 ns after the current starts which differs significantly from the experimental ~50 ns vaporization time that is observed with the Z-prepulse current rate of ~10 A/ns in [6]. An MHD simulation of a fast exploding W wire with current rise of ~10 A/ns is presented in [8]. The simulation results fit the experimental data, taking into account the metastable states of

liquid metal. However, this simulation [8] advanced only up to time of the voltage collapse, because the mechanism of breakdown is outside the scope of the MHD model.

In our paper we will present the set of experimental results obtained from fast (~150A/ns) and slow (~20A/ns) explosion of thin Al wires. The slow current rate corresponds to the prepulse current through a single wire in a typical (250-300 wire) wire array on a Z experiment [1,2]. The MHD simulations demonstrate quantitative agreement with electrical and optical diagnostics of fast exploding 25.4 μm Al wire. Moreover, the analysis of MHD simulations leads to important conclusions about the evolution of the parameters of the wire core and corona.

2. EXPERIMENTAL SETUP

2.1 Electrical diagram and diagnostics

The diagram of the experimental setup is presented in Fig. 1. A 100 kV Maxwell 40151-B (positive output) pulse generator with 7 nF capacitor bank, charging voltage 60 kV and stored energy of 12.6 J, provides the electrical pulse to drive the wire explosions. A 50 kV Maxwell 40168 trigger amplifier triggered the gas switch of the 100 kV pulse generator. Digital delay generator (Stanford DG-535) was used to synchronize the trigger amplifier with diagnostic devices. Jitter for the pulse generator was ~2 ns. A 9 m 50 Ω coaxial cable (RG 220/U) delivers the electrical pulse from the generator to the wire. The thin 10-38 μm diameter and 20 mm length Al wire (Aluminum alloy 5056: 5.2% Mg, 0.1% Mn, 0.1% Cr; room temperature resistivity ~6.0 μΩ·cm[1)]) was placed across a cathode-anode gap in the center conductor of the coaxial target unit. The assembly was evacuated to a pressure of ~10^{-4}-

[1)] Pure Al 99.99% has room temperature resistivity ~2.7μΩ-cm

10^{-5} torr to prevent gas breakdown. The scheme of vacuum chamber with coaxial target unit is presented in Fig. 2.

The experimental setup can operate in fast or slow mode. Typical waveforms for fast and slow explosion modes are presented in Fig. 3. In fast mode the current rate is ~150 A/ns into a short circuit (~3 kA maximum) and the voltage rate is ~12 kV/ns into an open circuit (~120 kV maximum). The slow-mode current rate is ~22 A/ns into a short circuit (~2 KA maximum) and voltage rate is ~1 kV/ns into an open circuit (~80 kV maximum). The ~100-ns oscillation period of the current is related to the impedance mismatch presented by the coaxial target unit. It is not relevant since energy deposition and wire explosion occur during the first 50 ns. The slower rise is typical for prepulse through individual wires on the Z-machine at Sandia National Laboratories (~30-45 A/ns).

The position of electrical monitors is shown in Figs. 1 and 2. The downstream current through the wire was measured with a 2 GHz bandwidth 0.1 Ω coaxial shunt resistor. The anode-ground voltage was measured with the capacitive divider; the inductive coil measured total upstream current. These electrical diagnostics provide upstream and downstream current, the voltage, the load resistance, and the joule energy deposition into the wire throughout the wire explosion. A Si PIN-diode with 1-ns rise time (ThorLabs DET210) monitored light emission power from the exploding wire. Streak camera (Hamamatsu C1587-01) radius-time (RT) diagrams of the exploding wire were obtained using a high-power pulse diode laser back lighter (Power Technology, IL30C, 905nm, 10W, 200ns) and appropriate relay optics. RT-diagrams provide the wire core expansion velocity and indicate the moment when expansion starts. Open-shutter visible light CCD images of the exploding wire show the 2D structure of the deposited energy. A stimulated Brillouin scattering (SBS)-compressed Nd:YAG (yttrium aluminum garnet) Q-switch laser with 120 mJ at 532 nm with 150 ps pulse duration (Ekspla

SL312) produced shadowgraphy, Schlieren and interferometric images of the exploding wire. All electrical waveforms are captured by a 4-channel, 1 GHz digital scope (Tektronix TDS 684C, 1 GHz, 5 GS/s). Time axis of the scope was cross-correlated with streak camera RT-diagram using the camera's synchropulse.

2.2 Interferometric measurements of atomic and electronic densities.

To reconstruct the atomic and electronic density we used shearing air-wedge interferometry first described [9] with short-pulse laser backlighting. Assuming comparable contribution of the free and bounded electrons, the interference phase shift δ can be written:

$$\delta(y) = 2\pi\alpha/\lambda \int N_a dx - 4.49 \cdot 10^{-14} \lambda \int n_e dx \qquad (1)$$

where α is the polarizability in cm^3; λ is the wavelength in cm; N_a and n_e the atomic and free electron densities in cm^{-3}; x is a coordinate along the probing direction, and y is the coordinate normal to the wire axis and probing direction.

Equation (1) has 3 unknowns (α, N_a, and n_e) and cannot be solved directly. Three cases exist for which we can reconstruct electronic or/and atomic densities. In the first case, when the free electron refractivity significantly exceeds the atomic/ionic refractivity, we can simplify equation (1) and recover electron density n_e using one-wavelength interferometry. This is the case for high temperature fully ionized plasma. In the second case, when atomic refractivity significantly exceeds the free electron refractivity, we can neglect the free-electron component of (1) and reconstruct the quantity αN_a using only one-wavelength interferometry. This is the case for low-temperature plasma and gas. Moreover, when the wire is totally vaporized, we can split N_a from α. This is possible because for totally vaporized wire we can write a second equation that describes the known linear density:

$N_{LIN}=N_{a0}\cdot\pi r_w^2=\int\delta(y)dy=2\pi\alpha/\lambda\iint N_a dxdy$, where N_{a0} is metal's initial solid-state density in cm^{-3}, and r_w is initial diameter of the wire in cm. In the third case, when atomic and electronic refractivity are comparable, it is necessary to use two-wavelength interferometry to reconstruct n_e, and αN_a (or n_e, α and N_a assuming total vaporization of the wire). We will present a detailed report of the results of two-wavelength interferometry in a future paper.

2.3 Measurements of resistive voltage.

In experiments with fast-rising current it is very important to inductively correct the measured voltage to reconstruct the resistive voltage. The measured voltage U can be written in the form:

$$U = U_R + U_L = IR + \left(L\frac{dI}{dt} + I\frac{dL}{dt} \right) \qquad (2)$$

where $U_R=IR$ is resistive voltage; U_L is inductive voltage, L the inductance, I the current, and R is the resistance.

To obtain the inductance for the coaxial target unit the wire is replaced by a 3 mm diameter copper wire to provide a short-circuit load for the full-pulse duration. The waveforms of voltage, current and reconstructed inductive voltage are presented in Fig. 4(a). The best fit for inductive voltage $L\cdot dI/dt$ was obtained for L=55 nH. For the experiment with thin wire it is necessary to take into account the additional self-inductance of the wire [10]:

$$L_w = 2l\cdot\ln\left(D/d_w\right) \qquad (3)$$

where l is the wire length and d_w the wire diameter, in cm; D is diameter of coaxial ground cup in cm, and L_w is the wire inductance in nH. For $D=5$ *cm*, $d_w=10$ μm and $l=2$ *cm* the wire inductance $L_w=34$ *nH*. Inductance of 3 mm diameter shunt $L_{shunt}=11$ *nH*. It means that the inductance of the coaxial target unit $L_0=L-L_{shunt}=44$ nH. Hence, the inductance of thin wire L_w

is comparable to the inductance of the coaxial target unit L_0 and must be taken into account for calculation of the resistive voltage.

For an exploding wire we assume a simple "dynamic model" of the inductance: before breakdown ($t<t_0$) inductance equals L_0+L_w; during breakdown ($t_0<t<t_1$) the inductance drops linearly from L_0+L_w to L_0 due to the fast radial expansion of conductive corona; and, after breakdown ($t>t_1$) the inductance equals L_0. This model gives an appropriate description of the behavior of the inductance, taking into account its fast drop during breakdown.

Figure 4(b) shows current and voltage waveforms for a typical fast exploding Al wire. We can see that experimental voltage after breakdown becomes inductive because its shape matches the shape of the inductive voltage calculated from the current waveform. During the resistive phase (0-20 ns) the experimental voltage significantly exceeds the inductive component but the inductive correction is important during the breakdown time (25-30 ns). Recovering the resistive part of the voltage IR in formula (2) provides an accurate reconstruction of the deposited energy and wire resistance during heating.

3. EXPERIMENTAL RESULTS

3.1 Laser shadowgrams of explosion

A typical set of shadowgrams of slow exploding 20.3 μm diameter and 2 cm long Al wires is shown in Fig. 5. The time between the frames was nearly 100 ns. The exposure time for each frame was 150 ps at a wavelength of 532 nm. Deposited energy is 1-1.5 times the vaporization energy. The typical expansion velocity of the wire core is about 3.5 km/s at the anode and 2.5 km/s at the cathode. We can see that the expanded wire core exhibits strong axial stratification with spatial scale ~50-100 μm. The stratification of the extended wire core

has been observed in our experiments only when deposited energy into the metal core is enough for full vaporization.

This axial stratification of the expanding gas-plasma cylinder has not been previously reported. However, other researchers have reported the stratification of the liquid wire core. Three possible reasons for stratification of the liquid-state conductor have been proposed. One is related to the development of electro-thermal instabilities during wire heating [11]. The second one is related with development of MHD instabilities of the liquid conductor [12]. The third possible mechanism of wire stratification is tied to the generation of current vortex structure in the liquid wire, as described in [13].

If deposited energy is less than the vaporization energy the wire core becomes “foam-like” [6] or shows a sol structure [5]. We can see that in all shadowgrams in Fig. 5 the energy deposition increases from the cathode to the anode. The reason for this conical energy deposition is related to the “polarity effect” and is discussed elsewhere [14-16]. Another interesting feature is the shock wave structure near the anode and cathode. This shock wave is stronger at the anode. Shock waves result from collision of the fast-expanding low-density plasma shell from the exploding wire with the under-the-anode and under-the-cathode plasmas. The anode and cathode plasmas are created from collision of anode and cathode with electron and ion beams generated by vapor breakdown along the wire surface [16].

The typical shadowgrams of the fast (a) and slow (b) exploding 16 μm diameter and 2 cm long Al wires are presented in Fig. 6. Clearly, the wire exploded in the fast-pulse mode expanded significantly faster (4.8 km/s at the anode and 2.7 km/s at the cathode) than in the slow one (1.7 km/s at the anode and 0.5 km/s at the cathode).

3.2 Expansion of the plasma shell

The laser shadowgram and light-emission optical diagnostics allow estimating the velocity of expansion of the low-density plasma shell. Figure 7 shows shadowgrams of the single (a) and double (c) fast exploding 20.3 μm Al wires and corresponding open-shutter images (b) and (d). The two parallel wires are 2 mm apart. For the single wire (a) we can estimate expansion velocity from the position of the under-the-anode shock wave. It corresponds to 8.2 km/s for the corona and 5.5 km/s for the core at the anode. At the cathode end the velocities are 5.3 km/s for the corona and 3.5 km/s for the wire core. The conical structure of energy deposition in Fig. 7(a) results from time-dependent breakdown along the wire length [16] and is consistent with the open-shutter image of Fig. 7(b), which show enhanced energy deposition under the anode.

The explosion of the two parallel wires (Fig. 7(c) and (d)) gives an additional way for estimating the plasma shell velocity using the evolution of the light emission. We can see in Fig. 7(c) the disturbance of the refraction coefficient between the wires. It results from the collision of the two expanding plasma shells. No visible disturbance can be seen on the outer boundary of the wires where the plasma expands freely into the vacuum. The open shutter image of Fig. 7(d) shows strong light emission between the wires owing to enhanced energy deposition in the collisional region. Because of the conical energy deposition into the wire, the intensity of the light emission from the collisional region grows toward the anode.

Figure 7(e) shows the evolution of the light emission from single and double wires. Light emission in both cases is nearly the same up to the time t_1=120 ns. At this moment the light emission from two parallel wires grows beyond the single-wire output due to the collision of the plasma shells. This provides estimation for the velocity of the plasma shell at ~8.3 km/s which agrees with the shock wave-based estimation for the single wire of Fig. 7(a) (~8.2 km/s). It is interesting that the collisional radiation stops growing at $t_2 \sim 2t_1$. This

indicates that the radiation starts to drop when the plasma shell from one wire reaches the initial axis of the other wire. From this time the front of corona from one wire expands in the same direction as a corona from other wire. Subsequently, the collision velocity between two coronas abruptly drops and produces less light emission.

The velocity of the plasma shell recovered from optical diagnostics corresponds to a relatively high-density collisional fraction of the fast-expanding corona ($Na \sim 10^{18} cm^{-3}$). It is possible using measurements of current to obtain data on the very low-density collisionless part of the expanding corona ($Na \sim 10^{13}$-$10^{15} cm^{-3}$). This is very important because the spread of this extremely low-density plasma defines the dynamics of the conductive plasma radius and voltage collapse. Figure 8 shows the evolution of the input I_{in} and output I_{out} current for the fast exploding 25.4 μm Al wire. For the short circuit the output current equals the input current. For exploding wires the currents differ during the resistive part of the explosion. During the first 200 ns the input and output currents are equal; all input current flows through the wire from the anode to the cathode. After ~250 ns, however, the output current differs from the input by the radial current to the outer coax wall. By 500 ns all of the input current, which now equals the short-circuit current of Fig. 3(a), becomes radial current to the ground wall and the output current falls to zero. We interpret this behavior to indicate that a fast radially-expanding low-density conductive plasma cylinder from the exploding wire reaches the ground cup and current subsequently flows between the anode and ground through this radial path of lower inductance (see Fig. 2). Because the distance between the wire and the ground cup is 25 mm, current measurements give an estimate of the plasma velocity of ~50-100 km/s. This low-density corona velocity is an order of magnitude faster than we inferred for the high-density collisional plasma from optical diagnostics [17]. Similar experiments were done later at Cornell [18] and demonstrated a low-limit of the velocity of the expanding

Cu wire corona as 14 km/s. This was substantially less than in our measurements, probably due to their smaller charging voltage.

3.3 Optical spectroscopy

Light hydrocarbon impurities can play a very important role in electrical breakdown processes for exploding wires. The voltage collapse dynamics depends on the expansion velocity of the low-density conductive plasma shell, and lighter ion mass allows faster plasma expansion velocity. To learn what impurities might be present during explosion we apply optical spectroscopy. The typical time-integrated optical spectrum for a wavelength range of 4200-6700 Å is presented in Fig. 9. The spectrum includes a set of Al-II and Al-III ionic lines. Two of those lines 4f-5g (4479 Å) and 4p-4d (4529 Å) can be used to determine the electron temperature [19]. The ratio of these line strengths gives an estimate of electron temperature of ~4-6 eV. It is important that we can see the spectral lines of atomic H-I (6563 Å) and of ionic C-II (5890 Å) since we observe those same spectral lines for exploding W wires. Elucidating the contribution of hydrocarbons to the physics of electrically exploding wires is important and requires further careful quantitative investigation [15,20].

3.4 Correlation of the explosion waveforms

It is very important to understand at what moment the wire starts to expand. The streak image of the wire diameter and plot of cross-correlated waveforms of current, resistive voltage, light emission power and wire radius for fast exploding 20.3 μm Al wire are presented in Fig. 10. The streak-camera image of the cross-section of the wire was obtained midway between the anode and cathode. We can see that light emission and wire expansion start at the onset of the voltage collapse. Light emission reaches its maximum value of ~0.8 kW in 4 ns during the voltage collapse and then drops. The fast-rising light emission is

associated with the onset of ionization of the surrounding vapor. The decrease in light emission is related to fast expansion of the ionized plasma shell. Experimental results from other fast and slow explosions show that, while the total energy deposited into the wire can differ shot to shot, the time of wire expansion and light emission always occurs with the voltage collapse.

3.5 Interferometric measurements

Two-wavelength interferograms of exploding 25.4 μm Al wire for 532 nm (a) and 1064 nm (b) probing beams at 167 ns after the start of expansion (shot 0314-02) are presented in Figs. 11(a) and (b). It is obvious that the disturbance of the interference lines for the wavelength 532 nm is more than for 1064 nm. According to formula (1), this means that the contribution of bound electrons is important. The deposited energy into the wire core was ~5.8 eV/atom, about 1.8 times more than needed for vaporization (under constant pressure). The phase shift profiles taken from the same slice at z=3 mm from the anode for 532 nm and 1064 nm wavelength are presented in the Fig. 11(c). The phase shift of the 532 nm interference lines is more then 2 times higher than for the1064 nm lines. After Gaussian smoothing of the experimental phase shift, we did Abel inversion to recover local radial distributions of $N_a(r)$ and $n_e(r)$ from the integral distribution of $\delta(y)$ (see formula (1)). Figure 11(d) shows the radial distribution of the atomic (assuming total vaporization of the wire) and electronic densities as well as the ion charge. The profiles show that the higher-density expanded Al core consists of slightly ionized Al gas (Z~0.01). It is important that ionization Z increases toward the periphery (Z~0.2 for r=1.15 mm). This implies a skin current that flows mainly through the outer low-density part of the expanding wire. The reconstruction of the atomic polarizability gives $\alpha \sim 1 \cdot 10^{-23} cm^3$. This is nearly 50% above the tabulated ground-state value ($6.8 \cdot 10^{-24} cm^3$).

It makes sense because the expanded metal column consists of gas at high temperature (~0.2 eV), and contains many excited atoms, which exhibit polarizability that is higher than ground-state value.

Next we consider 2D distributions of the atomic density for exploding Al wires. The low ionization of the expanded Al column allows the neglect of the free-electron component of refractivity in formula (1). Figures 12(a) and (b) show the shadowgram and interferogram of an exploding 25.4 μm diameter and 2 cm long Al wire (shot 0314-02) at 167 ns after voltage maximum. We can see from shadowgram in Fig. 12(a) that wire expansion increases in the direction of the anode and that the wire core is axially stratified. In this case the deposited energy is sufficient for full vaporization of the wire core. Figure 12(c) shows the 2D distribution of the atomic density recovered from 15 different cross-sections of the interferogram of Fig. 12(b). The peak atomic density drops a factor of 2 from ~$4.3 \cdot 10^{19}$cm^{-3} at the cathode to ~$2.1 \cdot 10^{19}$cm^{-3} at the anode. The diameter of the expanded wire is ~2 mm at the cathode and ~3 mm at the anode. This growth of radial expansion is related to wire overheating that increases from the cathode to the anode due to the "polarity effect" described in [16].

3.6 Fast and slow explosion waveforms

Typical waveforms for current, resistive voltage and light emission for fast (shot 0301-03) and slow (shot 0306-04) exploding 20.3 μm Al wires are presented in Fig. 13(a) and (b). The dependence of the wire resistivity, magnetic field pressure, and light emission on deposited energy are presented in Fig. 13 for fast (c) and slow (d) explosions. In both cases strong light emission begins with the voltage collapse. The voltage collapse terminates the energy deposition and the current waveform then matches that of a short circuit. The

comparison of the electric power, cathode-anode resistance and deposited energy waveforms for fast and slow explosions is presented in Fig. 13(e). The electrical power waveform is similar to the voltage and peaks at ~70 MW for the fast explosion and ~16 MW for the slow. For fast explosions the effective heating time (full width of electric power) was ~12 ns, and for slow ~32 ns. The total amount of deposited energy was E_{max}=213 mJ/cm for fast explosions and E_{max}=109 mJ/cm for slow. Nearly twice as much energy can be deposited in a fast explosion than in a slow explosion. This ratio varies somewhat for different metals, but always exceeds one. The energy ratio for 20.3 μm Al wire, averaged over 6 explosions, was 1.7.

We estimate the resistivity of Al by neglecting the wire's thermal expansion. The part of the resistivity curve after maximum shown by the dashed line on Figs. 13(c) and 13(d) cannot be attributed to the wire resistivity because of voltage collapse. Before voltage collapse occurs we attribute the measured resistance growth to the wire resistivity dynamics (solid line on Figs. 13(b) and (d)). Wire resistivity grows after melting (10-25 μΩ·cm [21]) up to 116 μΩ·cm (R=72 Ω) at 4.9 eV/atom for fast explosions and 60 μΩ·cm (R=37 Ω) at 2.5 eV/atom for slow. According to aluminum resistivity data of M. Desjarlais [22] these values of maximum resistivity correspond to a temperature of ~2 eV for fast explosions and ~0.4 eV for slow ones at a normal density 2.7 g/cm^3. For the fast-explosion mode we observe higher resistivity and higher energy deposition before breakdown. Under fast explosion Al wire heats at significantly higher magnetic pressure than in the slow-explosion regime. For fast explosions the magnetic field pressure reaches ~512 MPa, and for slow only ~132 MPa (Fig. 13(c), 13(d)). These pressures correspond to upper limits of magnetic field, based on measured current and the original wire radius.

For high pressure comparable with the critical pressure, the boiling temperature of aluminum increases above its normal value of 0.24 eV up to the critical temperature of 0.69 eV [23]. The critical pressure for Al is estimated between 270 and 447 MPa [23]. Hence, for fast explosion we can assume that Al experienced a supercritical phase transition. In this regime of heating the boiling is totally suppressed and a phase transition from liquid to gas-plasma state occurs homogeneously, without phase separation. On the other hand, in the slow-explosion mode a magnetic pressure of 132 MPa, while causing a significant increase of the boiling temperature from its normal value, is insufficient for an overcritical phase transition.

3.7 Statistical trends

The dependence of the specific energy deposited vs. wire diameter for fast exploding Al wires is presented in Fig. 14(a). The energy was calculated up to the time of maximum resistance (E_R), when resistance has dropped to half its peak value (E_{core}), and to when the resistance has dropped down to 5% of its maximum (E_{max}). We hypothesize that E_{core} corresponds to the Joule energy deposited into the wire core. Later, we will show that MHD simulation supports this hypothesis within 5% accuracy. We can see in Fig. 14(a) that energy deposition increases with decreasing wire diameter from 40 to 20 μm. No dependence of deposited energy on wire diameter is apparent below 20 μm.

The dependence of the heating time and time of resistance collapse or breakdown vs. wire diameter is presented in Fig. 14(b). We calculate the heating time as the full-width (at 5%) of the electric power curve. The heating times for Al wires with diameter between 10 and 20 μm fall within the interval 10-14 ns. Above 20 μm the heating time increases strongly with increasing wire diameter and reaching 40 ns for 38 μm wire. This increasing of the heating

time accompanies a decrease of the specific energy deposition before the breakdown (Fig. 14(a)).

The dependence of total deposited energy and maximum wire resistance vs. wire diameter are presented in Fig. 14(c). We can see that wire resistance for d>20 μm is less than 50 Ω and resistance for d<20 μm exceeds 50 Ω. Because our circuit has a 50 Ω source impedance, thin wires (d<20 μm) overmatch the circuit and thick wires (d>20 μm) undermatch it. This possibly explains why under our experimental conditions thin wires absorbed more energy per atom than thick ones.

The dependence of peak electrical power and specific electrical power vs. wire diameter for fast explosions are presented in Fig. 14(d). The peak electrical power reaches a maximum of ~70 MW for 20 μm Al wire. This happens because the maximum resistance of 20 μm Al wire matches the 50 Ω source impedance of the circuit (see Fig. 14(c)). At the same time, the peak specific power monotonically grows with decreasing wire diameter. This implies that the number of atoms in the wire drops faster than power, resulting in higher specific power.

The dependence of the deposited specific energy E_{core} vs. maximum of electric field is presented in Fig. 15(a). All our experimental data show growth of the energy deposition (from 2 to 6.3 eV/atom) with increase of the electric field (from 6 to 36 kV/cm). Dependence of the maximum wire resistivity vs. deposited specific energy E_R is presented in Fig. 15(b). All experimental points show growth of the maximum wire resistivity with increasing deposited specific energy E_R. The scattering of the experimental data is probably related to differences in magnetic field pressure dynamics during wire heating. This conclusion is based on variations of the current shape for different shots.

Figure 15(c) demonstrates for both fast and slow exploding Al wires the dependence of the expansion velocities of the plasma shell and dense core on the deposited specific energy

E_{core}. We determine the plasma shell expansion rate from laser shadowgrams that a show shock-wave structure, as in Fig. 6. We find that increasing the deposited energy yields greater expansion velocities. The expansion velocity V_{core} for the Al wire core ($N_a \sim 10^{20} cm^{-3}$) and for the plasma shell V_{shell} can be approximated by the linear expressions:

$$V_{core} = 1.24 \cdot E_{core} - 1.30 \qquad V_{shell} = 1.84 \cdot E_{core} - 1.57$$

where velocity is in km/s; energy in eV/atom.

The plasma shell expands 1.5-1.7 times faster than the wire core. Note, that these velocities are inferred from laser shadowgram that respond only to plasma densities above $\sim 10^{18}$-$10^{19} cm^{-3}$. We believe from upsteam and downstream current measurements (see Fig. 8) that a fast and low-density plasma component also exists, expanding at least 10 times faster than the higher-density component that we see in laser shadowgrams.

Figure 15(d) presents the heating time and deposited specific energy E_{core} vs. the maximum value of the current density. Increasing current density leads to a decreasing of the heating time $t \sim 1/j^2$ and an increasing of the specific energy into the wire core. We observe this for both fast and slow explosions. Correspondingly, increasing current density increases the heating rate.

4. RESULTS of MHD SIMULATION

4.1 Basic approach

Much of the behavior observed in our exploding Al wire experiments results from an interplay of complex processes whose physics is outside the scope of the magnetohydrodynamic description. Nevertheless, it is instructive to explore the behavior produced by basic MHD simulation in which the set of dynamic equations comprising the MHD description are governed solely by an equilibrium equation of state (EOS) (density and

temperature-dependent pressure and specific internal energy) and electron transport models (density and temperature-dependent electrical conductivity, and thermal conductivity). The MHD equations [24] determine the rate of change of the mass density, fluid momentum density, energy density, and magnetic flux density (Faraday's law). The energy equation includes terms determined by thermal diffusion and the magnetic flux density (Joule heating), and the magnetic equation includes the magnetic diffusion term; hence, electron transport models govern these equations. The electric current applied to the system provides the time-dependent boundary condition for the magnetic equation through Ampere's law, neglecting the displacement current.

Possibly important physics missing from the MHD model includes coexisting multiple phases [25], the atomization process, vaporization kinetics, electron kinetics (non-fluid particle behavior), and nonequilibrium ionization processes. Comparing the results of basic resistive MHD calculations to detailed laboratory measurements shows us when conditions occur where missing physics might be important and would need to be included in subsequent simulations.

4.2 Code description

The simulations we discuss in this paper were done with the ALEGRA code [26]. Developed by Sandia National Laboratories, ALEGRA (Arbitrary Lagrangian Eulerian General Research Application) is an Arbitrary Lagrangian-Eulerian (ALE) finite element code in 1D, 2D, or 3D. It has traditionally emphasized large distortion and shock propagation problems. Designed to run on distributed-memory parallel computers, it offers a number of physics options that include hydrodynamics, solid dynamics, structural dynamics, non-ideal MHD with external circuit coupling, and radiation MHD (multi-group flux-limited radiation

diffusion). ALEGRA also correctly diffuses magnetic field across vacuum regions, so there is no need to include an artificial, low-density gas to define vacuum. Material models include various EOS models, electron transport and opacity models, constitutive, yield, plasticity, fracture, and burn models.

In our simulations we employ only the physics options of magnetic diffusion coupled with hydrodynamics and thermal conduction. Radiation transport is not included, but a multi-group emission model is used. This provides an opacity-dependent energy loss as if the material were radiating, but no reabsorption is considered. Therefore, emission occurs only when the opacity is low enough to allow escaping radiation, such as in the low-density ablation layer and corona. But note that how such radiation emitted by the hot corona might enhance ablation by interacting with the higher-density wire edge is not included in our simulations. We plan to investigate the possible effects of more detailed radiation processes in a subsequent study.

ALEGRA produces accurate results for numerous problems with known solutions; *e.g.*, impact generated shocks, and cold diffusion [27]. We have also found that it compares favorably with results of another proven MHD code for the exploding wire problem [28] in spite of a number of significant differences in technique.

The key to these simulations is the use of accurate EOS and electron transport tables. We use Los Alamos SESAME equation of state tables 3711 and 3719 [29] and accurate electron transport properties recently calculated by M. P. Desjarlais [22]. The benefit of using these tables was first demonstrated in simulations of vacuum transmission lines under conditions of extremely high current density [30]. The EOS pressure as a function of density and temperature includes a vapor dome under which the Maxwell construction has been imposed for each isotherm. The corresponding specific energy as a function of density and

temperature includes the enthalpies of fusion and vaporization for those phase changes at different pressures. We are aware that these EOS tables suffer from some deficiency in heat capacity, and also do not include negative pressures that should be associated with the cohesion of the solid material. Hence, some premature expansion before melt and slightly elevated temperatures at certain densities and pressures will occur. Ionization (a step in the determination of electrical and thermal conductivities) is determined strictly as a function of density and temperature, based on Desjarlais' blending of single-ionization Saha with pressure-ionization correction and Thomas-Fermi ionization equilibrium [22].

4.3 Comparison with experiment

Basic electrical measurements that characterize the exploding wire are the current I(t) through the wire and the voltage V(t) across it. The experimental current I(t) for the fast-exploding 25.4 μm Al wire was used to provide a magnetic field boundary condition for the ALEGRA simulation of that wire at a large value of radius (r = 3.7 cm). This simulation boundary is farther from the wire edge than the ground cup of the experiment (r = 2.5 cm, see section 3.2) and therefore avoids confusing boundary interactions for several hundred ns even for the fastest components. The known experimental boundary effects are therefore precluded, but this choice is consistent with the model's inability to include electron kinetics and the effect of radial electric field on breakdown. The computational mesh of 600 cells is uniform with δr = .0635 μm out to 3x the initial wire radius, r_0; variable zoning then covers the remaining region out to the boundary with an additional 500 cells. Halving δr of the cells covering the region from the axis to $r = 3r_0$ produces essentially the same simulation results; but courser radial zoning leads to qualitatively different results that no longer capture important features of the experiment. The reasons for this are discussed in section 4.4.2 below.

Only a single axial zone ($\delta z = 50\ \mu m$) is considered, so the simulations are by construction 1-D (radial) and axial structure observed in the experiment cannot be treated.

Figure 16 shows experimental waveforms for current and voltage and simulation waveforms for voltage and wire radius. The resulting simulation voltage waveform is fairly close to the experimental shape within 10-20% error and gives the correct time for the voltage maximum and collapse. We must point out here that the electron transport models in our simulation are based on pure elemental aluminum, while the more-resistive aluminum alloy 5056 was exploded in the experiments. The greater pre-melt resistivity of the alloy (see section 2.0) could easily account for the early voltage discrepancy shown in Fig. 16.

The simulation shows that the wire thermally expands slightly after 12 ns. This is just after melting at 11 ns (the lack of restoring force in the EOS we used for solid Al [29] did not lead to nonphysical expansion for this fast-explosion case). The simulation voltage exhibits a jump at melt corresponding to the 250% jump in Al resistivity for melt at standard pressure [23]. This large jump is typical for good room-temperature conductors such as aluminum, and is absent for the refractory metals such as tungsten.

The density and temperature-dependent resistivity model is appropriate for temperature just below T_{melt} and just above T_{melt}; but at $T = T_{melt}$ the first use of the larger liquid-phase resistivity would be in error since the model does not allow for the finite time required at $T = T_{melt}$ to deposit the heat of fusion (nominally 0.11 eV/atom, but our EOS requires 0.19 eV/atom for the pre-melt density of 2600 kg/m^3) necessary to achieve melt and the corresponding higher resistivity. During this time the resistivity should remain below the post-melt value. For large pre-melt Joule heating rate (0.1 eV/atom-ns at $T = T_{melt}$, as in our fast-explosion mode) the voltage jump should occur about 2 ns after T_{melt} is reached (12.6 ns) rather than at 11.0 ns as shown in Fig. 16. (Note that the voltage was calculated from

simulation data that was recorded every 0.1 ns) There is also the issue of knowing T_{melt} accurately for the given density and pressure. The resistivity model utilizes the Lindemann melt temperature [31], scaled to the solid-density handbook value of T_{melt} (=0.08 eV) [23] to provide the functional dependence on density. In our exploding wire regime the difference from the solid-density value is slight.

The experimental voltage pulse does not exhibit any voltage jump. We postulate that the real wire melts in spatial regions that attain melt conditions at different times, unlike the ideal simulated wire that homogeneously melts in bulk. This inhomogeneous melting spreads out the melt time of the whole wire, eliminating any observable voltage jump. Following the experimentally inferred resistivity over its expected range during melt as a function of deposited energy as in Fig. 13(c) indeed indicates that more than the specific heat of fusion was required to melt the full wire.

The wire begins to rapidly expand with constant velocity at the time of peak voltage at 18-19ns. This agrees well with experimental data (Fig. 10) that show the onset of fast wire expansion at voltage collapse. Note that we chose to start the simulation (t = 0 in Fig. 16) at the point t = 14 ns on the experimental waveforms of Fig. 10). Therefore, the experimental waveforms have been time-shifted back 14 ns for comparison with the simulation waveforms in Fig. 16. The expansion velocities for atomic density $10^{20}cm^{-3}$ (4.5 km/s) and $3\cdot10^{20}cm^{-3}$ (3.7 km/s), inferred from the simulation, are close to the experimental values 4.8 km/s at the anode and 3.9 km/s at the cathode.

The comparison for simulated and experimental radial distributions of the atomic density at 170 ns is presented in Fig. 17. The best-fitting result was obtained for the under-the-cathode (z = 1 mm) radial profile. Due to the “polarity effect” [16] the energy deposition increases from the cathode to the anode (for positive polarity explosion). In this case the 1D

simulation gives appropriate results close to the cathode, which is free of the "overheating" effects related to the external radial electric field [16]. The 2D reconstruction of the atomic densities for this shot was presented in Fig. 12. The simulation was designed to capture the corona formation, requiring calculations over sub-nanosecond temporal and sub-micron spatial scales. The detailed quantitative experiment-simulation agreement presented in Fig. 17, is therefore noteworthy, having been achieved for the hugely different scales of 150 ns (time after voltage collapse) and ~1 mm (spread of core at this late time).

4.4 Analysis of simulation data

4.4.1 Current Distribution

While the simulation wire current agrees with the experiment by construction, the spatial distribution of this current is an interesting simulation result that is unavailable experimentally. Snapshots of the enclosed current (circulation integral of $\mathbf{B}/\mu$) plotted as a function of radius, and showing the radius that encloses all material at the time, clearly illustrates how the current distribution evolves. There are basically three stages of current distribution, summarized by the three snapshots of Fig. 18: (a) **Stage 1 -** all current flows through original wire core; (b) **Stage 2** - current switches from core to corona, and (c) **Stage 3** - nearly all current flows through the outer corona while the central region is essentially a dielectric. Of course, the circulation integral remains constant with radius past the radius that encloses all the current at a given time. This radius also coincides with the radius that encloses all material early in the pulse ($t < 17$ ns) and after corona formation ($t > 19$ ns). As the ablation layer develops, between $t = 17$ and 19 ns, (transition between Stages 1 and 2) the total-material radius exceeds the total-current radius. Once the outer shell of the neutral ablation layer ionizes (19 ns), three radii describe the current distribution in Stages 2 and 3: the inner

radius of the neutral ablation layer (the radius that just encloses the core conduction region), the inner radius of the corona (outer radius of the ablation layer), and the outer radius of the corona (the radius that encloses the total current comprising core current plus corona current). The total-current radius and the total-material radius again coincide for the remainder of the pulse. In Stage 3 the core current is negligible compared to the corona current.

4.4.2 Corona formation

The simulation clarifies some significant points in the development of the corona, during the crucial period during the transition between Stage-1 and Stage-2 current distributions. Early in the pulse (11 ns) the wire melts, expands slightly but remains intact. The core starts to expand after 13 ns when hydro-pressure develops a stationary gradient that points radially inward (Fig. 19). A thin, nearly dielectric ($<Z> << 1$) outer layer develops when deposited energy reaches a value that is roughly 70% atomization enthalpy. This cold "ablation" layer is initially 1-2 μm thick. After t = 15 ns the core superheats ($T > T_c = 0.7$ eV) and still carries all the current. The ablation layer expands to a thickness of ~5 μm (still cold), then starts expanding adiabatically to ~10 μm. No atomization model is used, but the low-density cold dielectric layer develops consistently with the topology of the EOS energy surface. The pressure and specific energy points of the wire at a set of radial positions that scan the wire cross-section are plotted in Fig. 20 at three times during the development of the ablation layer. These sets of points constitute the phase portraits of the wire in the Pressure-Density and Energy-Density planes. Isothermal pressure and energy contours are shown in the background. The lower-pressure (and energy) points are at the outer radii of the wire. These portraits show that as the wire heats it becomes energetically possible to cool by expansion at

17 ns. Between 17 and 18 ns the outer portion of the dielectric layer starts expanding adiabatically.

The outer edge of the ablation layer (~10^{-6} of solid density) then becomes sufficiently resistive (10^8 x resistivity of stainless steel) so that, with the small but finite current density present there (~1 A/mm^2), a 1 μm thick layer rapidly (1 ns) Joule heats to ionization energy levels (~6 eV/atom). This layer subsequently conducts more current. The current density, J flowing through the layer increases by factor of 10^4 and conductivity, σ increases by factor of 10^5. Energy deposited into this newly created corona thus increases and the coronal periphery rapidly attains nearly full ionization levels. Note that the conductivity of the nascent corona is much less than the core conductivity.

An important question must be asked about the low-density edge of the "ablation" layer (0.001-0.01 kg/m^3): is the MHD approximation still valid? The answer is yes. Owing to the comparatively large volume of the cells at this radius (2π r δr δz), there are about 2x10^8 Al atoms/cell and 4 (at 1eV) to 12 (at 0.1 eV) Debbie lengths per δr. (In the corona-formation region, r is about 27 μm, δr = .0635 μm, δz = 50 μm). Clearly the cell volume would not be able to save the MHD approximation in a simulation that was highly resolved in all three directions.

It is also interesting to inquire whether the outer edge of the ablation layer that initially ionizes is spatially resolved, or is the ionization-layer thickness just δr. Again, the answer is yes, the initial ionization shell is resolved. At 19 ns the ionization layer is about 2 μm thick (31 cells). The very first instance of an ionization layer in the simulation occurs over a more limited number of cells or even just a single cell. At some radial point towards the axis, where J^2 is larger, the resistivity drops off sufficiently so the time integral of [σ^{-1} x J^2] is below

ionization levels for the same period (~1ns) that gives ionization the next cell out. This relationship determines the radial resolution required to capture the corona formation in the simulation by this simple mechanism that is based solely on the implementation of equilibrium EOS and electron transport tables. Corona formation can occur in the simulation only if the radial cells are sufficiently small at the edge of the ablation layer to allow an outer region where the time integral of $[\sigma^{-1} \times J^2]$ can reach ionization levels. Lagrangian simulations, where the cells covering the ablation region would be expanding during this phase of the simulation, cannot capture corona formation. A difficulty in our simulations is the small time step that is required for stability during the ablation-layer formation in the small cells. A large Alfven speed forces the time step to be in the 10^{-16} – 10^{-15} s range just prior to corona formation. The time step recovers to a more reasonable 10^{-14} – 10^{-12} s range after voltage collapse.

The Stage 2 current now flows both through the low-area, high-conductivity core and through the high-area, lower-conductivity corona. After 19.5 ns the corona rapidly expands and conducts more current than the core, while the core conductivity drops (but still exceeds the corona conductivity). The corona area rapidly increases for a dramatic drop in resistance. This is the time of the voltage collapse and the start of strong light emission observed experimentally. After the voltage collapses the corona carries essentially all the current (Stage 3). We need to emphasize that the geometrical drop of the coronal *resistance* rather than relative core-corona *resistivities* leads to the current transfer to the corona. During Stage 3 essentially no more energy is deposited into the core, and it expands at constant velocity. Between 18 and 21 ns, the minimum core resistivity is 200 to 700 μΩ·cm; while the corona expands with a nearly constant resistivity of 1400 μΩ·cm.

4.4.3 Conduction and Dielectric Radius Expansion velocities

From plots such as those of Fig. 18 a well-defined expansion velocity to consider in comparison with the experiment is the velocity of the outer edge of different conductance regions. As shown in Fig. 21 the radius that encloses the total current in Stage 3 has a constant velocity after 19.5 ns of 70 km/s. Experimentally, a velocity of between 50 and 100 km/s was inferred from upstream and downstream current measurements (Fig. 8). Laser probing shows that the wire core expands with v~ 4 km/s (at the cathode). This measurement matches the expansion velocity of the wire core, which Fig. 21 shows is 4.2 km/s. This simulation velocity corresponds to an energy of 3.5 eV/atom deposited into the core. Atomization enthalpy (not included in our EOS) is 3.2 eV/atom, so experimentally we expect to see about 6-7 eV/atom deposited into the core by the time of corona formation. In fact, as Fig. 14a shows that 5.8-6.5 eV/atom was observed for 25.4 μm diameter wire, Note these expansion velocities remain constant for 100's of ns. These energetic expansions, much faster than thermal diffusion speeds, constitute the explosion of the wire.

4.4.4 Phase trajectories

It is instructive to view snapshots of the phase points of the wire, plotted parametrically in radius (as done in Fig. 20), as they evolve on the respective EOS surfaces. We can consider the (ρ, T, P) phase points on the EOS pressure surface, or the (ρ, T, σ) points on the conductivity surface. A sequence of the (ρ, T, P) snapshots is shown in Fig. 22, and corresponding (ρ, T, σ) snapshots in Fig. 23. For convenience of scale the conductivity surface plot is cutoff from below at a fairly large value; the conductivity actually becomes infinitesimally small with a huge gradient in the low-density/low-temperature region. The outline of the vapor dome (binodal curve, sketched explicitly in Fig. 22a) can be discerned on the shaded pressure surface plots. Under the vapor dome the spinodal boundary curve (where

$(\partial P/\partial \rho)_T = 0$) is shown for reference. The present simulations did not employ any special modifications to properly model metastable behavior near the spinodal. Behavior of metastable liquid might be important, especially for slow-exploding refractory metals such as tungsten, and is an area of active research [8,32].

Initially, the collection of phase points for the wire overlay compactly on the EOS pressure surface. Since the pressure gradient with density in the solid phase is very large the phase points spread out in pressure as small-amplitude density waves travel across the wire during initial Joule heating. Hence it is informative to plot the phase points with a range of colors that maps to the value of the radius for that point. This color map is shown for reference above each snapshot, and must cover larger radial ranges with increasing time. As the set of phase points reaches the liquid side of the vapor dome the pressure reversal on axis shown in Fig. 19 is indicated (14 ns); note that the ~zero pressure dip seen on the linear scale of Fig. 19 is actually 0.03 kbar. Shocks directed inward from the heated wire's surface converge on axis during melt, peaking the axial pressure well above the critical pressure. At 14 ns the shocks are moving away from the axis reversing the pressure gradient, and by 15 ns the pressure is again maximum on axis, and the center of the wire again attains high pressure as it travels over the critical point between 16 and 17 ns. At this time the low-density edge (ablation layer) develops and progresses down the vapor side of the dome. Between 18 and 19 ns the outer edge of the ablation layer ionizes as described previously. This region of the wire traverses a long path on the pressure surface and corresponds to an increasingly large radial extent with time. Once the corona carries most of the current, the core expands adiabatically along the vapor side of the dome (t > 20 ns).

Viewing the corresponding (ρ, T, σ) points at the time of corona formation in Fig. 23 illustrates a key feature of this system: the cold, high-density (compared to the coronal

plasma) material of the ablation layer falls near the metal-insulator transition of Al where the gradients of conductivity with density and, below the transition, with temperature are exceedingly great. Therein lies the reason for the sensitivity of exploding wire simulations to details of the EOS. Slight differences in EOS can change the density and temperature of the outer layer of the wire slightly, but enough to change the conductivity sufficiently to prevent Joule heating from reaching ionization levels at the appropriate experimental time, or at all.

4.4.5 Pressure and Boiling

Summarizing some of the phase information shown in the snapshots of Fig. 22, the time-dependence of the radial average of the hydro pressure profile is presented in Fig. 24(a). Time-dependence of the radial average of the magnetic pressure profile is also presented for comparison. The superposition of the applied electrical power, the melting time, and the time-dependent wire radius (later becoming core and corona radii) allows a correlation of features in the pressures with important times in the exploding wire evolution. The magnetic and hydro pressures are comparable early in the current pulse; but during melt both pressures peak, the magnetic at about the critical pressure, and the hydro at 10x critical pressure. Melting coincides with Joule-heating-induced shock propagation from the edge of the wire. The pressure wave peaks at the center and just as quickly drops to zero there (see Fig. 19); the average pressure then rises to a new peak of 5x critical pressure during the ablation. With the establishment of the corona ($t > 20$ ns) the magnetic pressure becomes insignificant since most of the current is flowing at a large radius in the expanding corona.

Viewing snapshots of the radial profile of the hydro pressure during the important corona-formation period reveals in Fig. 24(b) the “pressure-cooker” nature of the explosion process. Vaporization of interior regions of the wire, or “boiling”, is a possibly important mechanism in the electrical explosion of wires [32]; however, in our case, for nanosecond

explosion of aluminum, the simulation suggests that hydro pressure prevents vaporization throughout the wire interior. Vaporization can occur only at the wire's edge where pressure is negligible. This phase change constitutes "ablation" rather than "boiling".

4.4.6 Evolution of various radial profiles

Figure 25(a-f) demonstrates the simulated radial profiles at several different times (5, 10, 20, 30 and 40 ns) for atomic density (a), current density (b), magnetic field (c), hydro pressure (d), temperature (e) and ionization (f). Before corona formation or "breakdown" the current flows through the wire and heats it homogeneously. During breakdown we can see the creation of the low-density corona with $Na \sim 10^{14}$-$10^{18} cm^{-3}$ and the switching of the current from wire core to the corona. It is interesting that just prior to the time of experimental breakdown the simulation predicted the existence of the non-conductive dielectric layer. After breakdown the current is rejected from the wire core in favor of the corona. The energy deposition to the core terminates due to the fast-expanding radius of conductivity (~70 km/s). Because the Spitzer resistivity of low-density ($Na \sim 10^{14}$-10^{16} cm^{-3}) and high temperature Al plasma is 100-1000 $\mu\Omega \cdot cm$ (which is 100-1000 times that of room-temperature metal) the fast voltage collapse in 5 ns can be explained only by the fast expansion of the corona. The current density has its maximum value in the wire core ~300 MA/cm^2 before the breakdown. After breakdown current density in the corona drops from 10 to 0.1 MA/cm^2. The simulation demonstrates the existence of high temperature, ~50-100 eV, in the corona with ionization ~10. The evolution of the radial profiles shows that after breakdown the exploding wire evolves into a two-phase object: cold and high-density wire core and hot and low-density corona.

4.4.7 Core-Corona dynamics

Figure 26(a-f) demonstrates evolution of the different parameters for wire core and corona: splitting of the current between wire core and corona (a), electrical power (b) and specific electrical power (c) applied to core and corona, the conductive corona radius ($Na \sim 10^{14} cm^{-3}$) and radius of the wire core ($Na \sim 10^{20} cm^{-3}$) (d), the maximum temperature for wire core and corona (e), and the linear density for wire core and corona in (f). Because we know from simulation how current splits between wire core and corona, and the radial profile of atomic density, we can derive the amount of energy deposited into the wire core and corona. For this calculation we used the experimental voltage waveform. Energy deposition into the corona occurs up to the time of breakdown. The total value of the energy deposited into the wire core is 270 mJ/cm, and into the wire corona is 60 mJ/cm. The corresponding specific energy deposited into the wire core is 5.5 eV/atom, and into the corona is 2.5 keV/atom. This large difference in energy-per-atom is due to the extremely small mass of the corona. Figure 26(f) shows that corona contains only 0.1-0.2% from the wire mass. For 25 μm diameter Al wire it is necessary to vaporize only ~30 monatomic layers. It is clear now, that under such conditions any hydrocarbon impurities would play an important role in the breakdown process. The coronal expansion velocity is ~70 km/s (the velocity of the point where $Na \sim 10^{14} cm^{-3}$), and core expansion ~4.5 km/s ($Na \sim 10^{20} cm^{-3}$). Different density layers expand at slightly different velocities, with lower densities faster. Recall that the velocity of the conductive edge of the core and corona (these edges include the fastest low-density components) is comparable to or slightly exceeds the constant-density velocities: 70 km/s corona, and 5 km/s core. Fast expansion of the conductive outer radius results in voltage collapse and termination of the energy deposition into the wire core.

The temperature of the wire core increases up to ~1.3 eV (~5.5 eV/atom deposited energy) at 19 ns and subsequently drops to 0.5 eV by 40 ns due to adiabatic cooling of the

expanding wire core. The temperature of the corona rises to ~130 eV in 1-2 ns during voltage collapse and drops to 30-40 eV by 40 ns owing to fast plasma expansion. The plasma cooling exceeds Joule heating because of the rapidly falling resistance of the cathode-anode gap due to fast corona expansion.

5. SUMMARY

Summarizing our experimental and theoretical results: **(1)** Before the voltage collapse the current flows through the entire wire cross-section and quasi-homogeneously heats it. The hydro-pressure of tens of kbar range is large enough (critical pressure 3-5 kbar) to prevent the hot liquid wire core from boiling. **(2)** After melting the liquid Al wire starts vaporizing and an expanding vapor cylinder surrounds the wire core. Simulation shows that high temperature and low density subsequently create the condition for vapor ionization. This is sufficient to explain the corona formation near the cathode (see Fig. 17) where the radial electric field [16] is negligible and the 1-D quasi-equilibrium fluid description is accurate. In the real experimental system the influence of the radial electric field on electronic emission from the wire surface is a critical feature that precipitates vapor ionization [16]. **(3)** Part of the current starts to flow through the ionized vapor and swiftly Joule heats it to ~100 eV. Such a large temperature rise is related to the very small amount of wire mass involved in ionization (~0.1% of wire mass). For 25 μm Al wire 0.1% of the mass is concentrated into $\delta r \sim 6.5$ nm of the wire surface (~25 mono atomic layers). Fast voltage collapse is contingent on the plasma corona's high-velocity (~100 km/s) expansion.

Three main conditions must exist for voltage collapse in exploding wires: first, a vapor environment must surround the hot wire; second, the vapor must ionize; and third, the ionized vapor (corona) should be able to rapidly expand. The absence of any of these conditions

would preclude voltage collapse. For example, no voltage collapse is observed for exploding wires in air at normal pressure owing to retardation of the corona expansion.

The moment of voltage collapse is very important in the physics of exploding wires. The voltage collapse terminates energy deposition to the wire core and provides a natural barrier to limit rising temperature [4]. During breakdown the current switches from the high-density wire core to low-density and fast-expanding corona in ~5 ns. Because the resistivity of the corona exceeds the resistivity of the hot metal (for 10-100 eV temperatures the low density plasma resistivity is 100-1000 μΩ-cm), the switching of the current to the corona is related to its fast expansion but not to its high conductivity. For a low density corona that expands with a velocity of 50-100 km/s the cathode-anode resistance can drop to less than 1 Ω in ~5 ns.

The energy deposition into the wire core terminates at a level of a few eV/atom, and for the corona a few keV/atom. After breakdown the wire becomes a heterogeneous object: hot (~100 eV), low-density (~10^{15} cm^{-3}), fast expanding (~100 km/s) corona and a cold (~1 eV), high-density (~10^{22} cm^{-3}), slow expanding (~1 km/s) core. The core expands at about the sound speed. The wire core exists as strongly coupled plasma, while the corona is an ideal plasma. After breakdown the wire core expands and adiabatically cools. Fast expansion of the hot corona also results in its cooling. In this case the temperature cannot be supported by Joule heating because of the rapidly falling cathode-anode resistance due to fast expansion of the conductivity radius.

The wire core after voltage collapse can be in any of three main states: solid, micro-drops or gas-plasma [33]. Which condition dominates depends mainly on the amount of deposited energy before voltage collapse. The expanding gas-plasma core of an overheated Al wire becomes stratified with a ~100 μm period.

In conclusion, we want to point out that 1D MHD simulation using the ALEGRA code with reasonably accurate equilibrium EOS and resistivity provides an accurate description of the nanosecond explosion of the Al wire. The simulation gives good agreement for the main parameters of explosion and gives important predictions for the set of parameters that cannot be measured directly in experiments. The next important step for computer simulation is the description of the initial stage of electrical explosion of refractory-metal wires like W. The sophistication of this problem is demonstrated in [16,34] regarding the possibility of a “cold” regime of explosion due to hydrocarbon impurities, the importance of electronic emission on triggering vapor ionization, and the inhomogeneous energy deposition along the wire length due to the Schottky effect.

ACKNOWLEDGEMENTS

The authors gratefully acknowledge H. Faretto, A. Oxner, W. Brinsmead and A. Astanovitskiy for technical assistance on experiment. We also wish to acknowledge the work of Dr. T.A. Haill and the ALEGRA code development team at Sandia National Laboratories, and Dr. T.A. Mehlhorn for his support and technical leadership of the team. Special thanks go to Drs. P.V. Sasorov, A.D. Rakhel, M.P. Desjarlais, E.Waisman, and J.S. DeGroot for useful discussions. We thank Dr. B.M. Jones for his thoughtful reading of our manuscript that helped us improve its clarity. The experimental part of this project has been supported partially by DOE-NV, DOE-EPSCoR, SNL, UNR and Cornell University. Sandia is a multiprogram laboratory operated by Sandia Corporation, a Lockheed Martin Company, for the United States Department of Energy under Contract DE-AC04-94AL85000.

REFERENCES

1. T. W. L. Sanford, G. O. Allshouse, B. M. Marder, et al., Phys. Rev. Letters **77**, 5063 (1996).
2. R. B. Spielman, C. Deeney, G. A. Chandler, et al. Phys. Plasmas **5**, 2105 (1998).
3. F. N. Beg, S. V. Lebedev, S. N. Bland, et al., Physics of Plasma **9**, 375 (2002).
4. F. D. Bennett, in *Progress in High Temperature Physics and Chemistry*, **2**, 1-65 (1968).
5. S. V. Lebedev, A. I. Savvatimskii, Usp. Fiz. Nauk **144**, 215 (1984) (in Russian) [Sov. Phys. Usp., **27**(10), 749 (1984)].
6. D. B. Sinars, T. A. Shelkovenko, S. A. Pikuz, et al., Physics of Plasmas **7**, 1555 (2000).
7. J. P. Chittenden, S. V. Lebedev, J. Ruiz-Camacho, et al., Phys. Rev. E **61**, 4370 (2000).
8. S. I. Tkachenko, K. V. Khishchenko, V. S. Vorob'ev, et all, Teplofiz. Vysok. Temp. **39**, 728 (2001) (in Russian) [High Temperature **39**, 674 (2001)].
9. G. S. Sarkisov, Prib. Tekh. Eksper. **39**, 110 (1996) (in Russian) [Instrum. Exper. Tech. **39**, 727 (1996)].
10. L. D. Landau, E. M. Lifshitz, and L. P. Pitaevskii, *Electrodynamics of Continuous Media*, (Butterworth-Heinemann Ltd.) 1984.
11. F. D. Bennett, H. S. Burden and D. D. Shear, J. Appl. Phys. **45**, 3429 (1974).
12. A. A. Valuev, I. Y. Dikhter, and V. A. Zeigarnik, Zh. Tekh. Fiz. **48**, 2088 (1978) (in Russian) [Sov. Phys.- Tech. Phys. **23**, 1190 (1978)].

13. N. B. Volkov, N. M. Zubarev, and A. M. Iskol`dskii, Zh. Eksp. Teor. Fiz., **109**, 429 (1996) (in Russian) [J. Exp. Theor. Phys., **82**, 228 (1996)].

14. G. S. Sarkisov and D. McCrorey, IEEE TPS **30**, 98 (2002).

15. G. S. Sarkisov, S. E. Rosenthal, K. W. Struve, et al., in *Dense Z-Pinches: 5th International Conference on Dense Z-Pinches*, edited by J. Davis, C. Deeney and N. Pereira (AIP Conf. Proc. 651, Albuquerque, NM, USA, 2002), p. 209 and p. 213.

16. G. S. Sarkisov, P. V. Sasorov, K. W. Struve, et. al., Phys. Rev. E **66**, 046413 (2002).

17. G. S. Sarkisov, B. S. Bauer, P. V. Sasorov, et al., in *28th IEEE International Conference on Plasma Science* (Las Vegas, NV, USA, 2001), p. 148.

18. P. U. Duselis and B. R. Kusse, Physics of Plasmas **10**, 565 (2003).

19. H. Griem, *Plasma Spectroscopy* (Academic Press, NY, 1964); C. Christou, IEEE TM **31**, 689 (1995).

20. T. S. Strickler, M. D. Jonston, R. M. Gilgenbach, et al., Bulletin of the American Physical Society, DPP 2002, Vol. **47**, No. 9, p. 242.

21. G. T. Dyos and T. Farrell, *Electrical Resistivity Handbook* (London: Peter Peregrinus, 1992) p. 39.

22. M. P. Desjarlais, Contrib. Plasma Phys. **41**, 267 (2001).

23. Handbook of Physical Quantities, *edited by I.S. Grigoriev and E.Z. Melikhov* (CRC Press, 1997) p. 395.

24. N. A. Krall and A. W. Trivelpiece, *Principles of Plasma Physics*, (McGraw-Hill, New York), 1973.

25. A. D. Rakhel and G. S. Sarkisov, accepted in Int. J. Thermophysics, 2004.

26. *"ALEGRA: User Input and Physics Descriptions – October 1999 Release"*, Edward A. Boucheron, et. al., SAND99-3012, SNL, Albuquerque, NM.

27. "*Physics Applications in the ALEGRA Framework*", M. K. Wong, J. R. Weatherby, C. D. Turnerb, A. C. Robinson, T. A. Haill, and D. E. Carroll, Sandia National Laboratories Report, SAND2001-0905A.

28. "*Equation of State and Electron Transport Effects in Exploding Wire Evolution*", S. E. Rosenthal, M. P. Desjarlais, and K. R. Cochrane, PPPS-2001 Pulsed Power Plasma Science 2001 Digest of Technical Papers, R. Reinovsky and M. Newton, Eds., p. 781.

29. http://t1web.lanl.gov/home/t1/newweb_dir/t1sesame.html; G. I. Kerley, T. L. Christian -Frear, "Sandia Equation of State Data Base", SNL Report SAND93-1206, 1993; K. S. Holian, T-4 Handbook of Material Properties Data Base, LANL Report LA-10160-MS, 1984;

30. S. E. Rosenthal, M. P. Desjarlais, and K. R. Cochrane, Pulsed Power Plasma Science 2001, IEEE Catalog No. 01CH37251, p. 781.

31. P. Papon, J. Leblond, and P. H. E. Meijer, *The Physics of Phase Transitions*, (Springer-Verlag, Berlin, 1999), p. 90.

32. M. M. Martynyuk, Zh. Tekh. Fiz. **44**, 1262 (1974) (in Russian) [Soviet Physics - Technical Physics, **19**, 793 (1974)].

33. G. S. Sarkisov, K. W. Struve, D. H. McDaniel, submitted to Phys. Rev. E, (2004).

34. G. S. Sarkisov, B. S. Bauer, and J. S. DeGroot, Pis'ma Zh. Eksp. Teor. Fiz. **73**, 74 (2001) [JETP Letters, **73**, 69 (2001)].

FIGURES CAPTIONS

Fig. 1 Electrical diagram of the experimental setup.

Fig. 2 Vacuum chamber with coaxial target unit.

Fig. 3 Long time-scale waveform of the current on a short circuit (a); short time scale waveform of the fast and slow current on a short circuit (b); short time-scale waveform of the fast and slow voltage on open circuit (c).

Fig. 4 Short-circuit waveforms for current, voltage and inductive voltage for Lo= 50 nH (a). Exploding-wire waveforms for current, voltage and inductive voltage for Lo= 50 nH (b).

Fig. 5 Set of laser shadowgrams of slow exploding Al wires (20.3 μm diameter and 2 cm length) at different times.

Fig. 6 Shadowgrams of the fast (a) and slow (b) explosion of 16.2 μm diameter and 2 cm long Al wires.

Fig. 7 Shadowgram (a) and open-shutter (b) images of single fast exploding 20.3 μm Al wires. Shadowgram (c) and open-shutter (d) images of two parallel fast exploding 20.3 μm Al wires (2 mm distance between wires). (e): Evolution of the light emission for single (a,b) and two parallel (c,d) wires.

Fig. 8 Evolution of the upstream and downstream current for fast exploding 25.4 μm Al wire.

Fig. 9 The time-integrated optical spectra of the fast exploding 10 μm Al wire.

Fig. 10 Streak shadowgram image with 905 nm laser backlighter of the fast exploding 20.3 μm Al wire and appropriate waveforms of the current, voltage, light emission and wire radius. Light emission and wire expansion starts at the moment of surface breakdown.

Fig. 11 Two-wavelength interferograms of fast exploding 25.4 μm Al wire (a,b) at 167 ns. Interference phase shift in cross-section A-A (c). Radial distribution N_a, n_e and Z for cross-section A-A (d).

Fig. 12 Shadowgram (a) and interferogram (b) of 25.4 μm diameter and 2 cm length Al wire at 196 ns after voltage maximum. Probing wavelength is 532 nm. 2D distribution of the atomic density (c) recovered using Abel inversion procedure.

Fig. 13 Typical waveforms of current, voltage and light emission for fast (a) and slow (b) exploding 20.3 μm Al wires. Recovered distributions of the wire resistivity, magnetic field pressure and light emission vs. deposited energy for fast (c) and slow (d) explosions. Evolution of the electrical power and deposited energy for fast and slow explosions (e). Long time scale evolution of the light emission for fast and slow explosions (f).

Fig. 14 Specific energy deposition vs. wire diameter (a). The time of wire heating and time of breakdown vs. wire diameter (b). Total deposited energy and wire maximum resistance vs. wire diameter (c). Electrical power and specific electrical power vs. wire diameter. All plots are for the fast-explosion mode.

Fig. 15 Dependence of the specific energy deposited into wire core vs. maximum value of the electric field (a). Maximum wire resistivity vs. deposited specific energy (b). Velocity of the expanding plasma shell and wire core vs. deposited specific energy (c). Dependence of heating time and deposited specific energy on the maximum current density (d).

Fig. 16 Waveforms for current and voltage taken from the experiment, and simulated voltage (dashed curve), and wire radius (o) for fast exploding 25.4 μm Al wire. The gray shaded region shows the velocity of the expansion of the wire core under the anode and the cathode.

Fig. 17 Experimental and simulated radial distributions of the atomic density for 160ns after voltage maximum.

Fig. 18 Three basic stages of current distribution in fast exploding aluminum wire: **Stage 1**- current flow through the wire core (a); **Stage 2**- current switching from core to corona (b); **Stage 3**- current flow through the corona (c).

Fig. 19 Time and space-dependence of post-melt hydrodynamic pressure (a), time-dependence of axial pressure (b). Critical pressure is ~2.7-4.5 kbar.

Fig. 20 Wire phase portraits at 15, 17, and 18 ns: (top) Pressure-density plane, (bottom) Specific energy-density plane.

Fig. 21 Time-dependent conductive-radius and material-radius velocities obtained from enclosed current snapshots.

Fig. 22 Wire phase portraits on the EOS pressure surface at t = 14, 15, 17, 18, 19, 20, 30, 60, and 120 ns.

Fig. 23 Wire phase portraits on the conductivity surface at t = 14, 15, 17, 18, 19, 20, 30, 60, and 120 ns.

Fig. 24 Evolution of the electrical power, isolines of atomic density, average hydro and magnetic pressures (a). Radial profiles of hydro pressure during voltage collapse time (b).

Fig. 25 Simulation radial profiles at different times (5, 10, 20, 30, 40 ns) for atomic density (a), current density (b), magnetic field (c), hydro-pressure (d), temperature (e), and ionization (f).

Fig. 26 Results of simulation summarizing core-corona evolution: current splitting between wire core and corona (a); evolution of the electrical power (b) and specific power (c) for wire core and corona; evolution of the radius for wire core and corona (d); evolution of the maximum temperature for wire core and corona (e); evolution of the linear density for wire core and corona (f).

SAND2004-2869
Printed June 2004

Figures for the paper:

Nanosecond Electrical Explosion of Thin Aluminum Wire in Vacuum: Experimental and Computational Investigations

G.S. Sarkisov, S.E. Rosenthal, K.R. Cochrane,
K.W. Struve, C. Deeney, and D.H. McDaniel

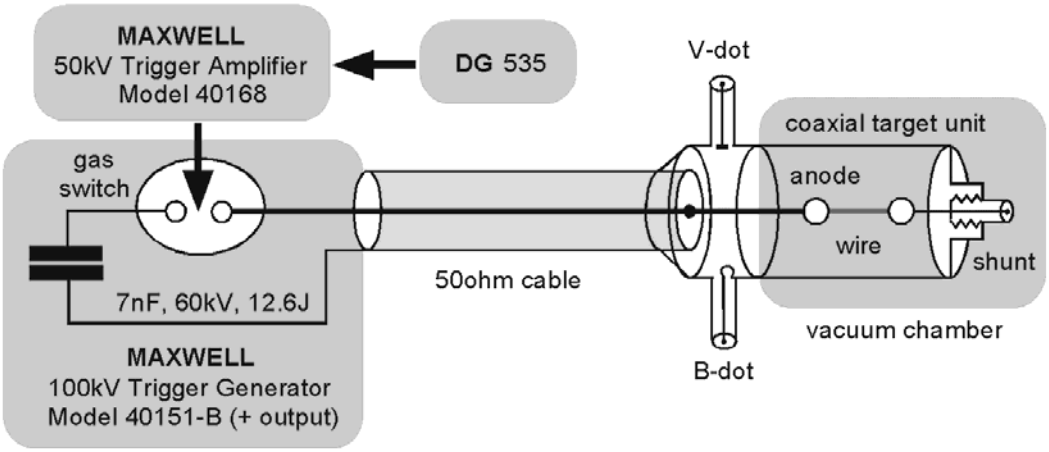

Fig. 1 Electrical diagram of the experimental setup.

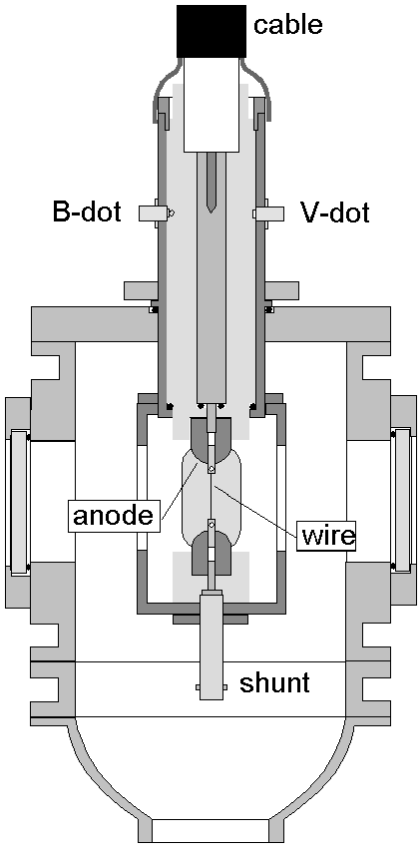

Fig. 2 Vacuum chamber with coaxial exploding unit.

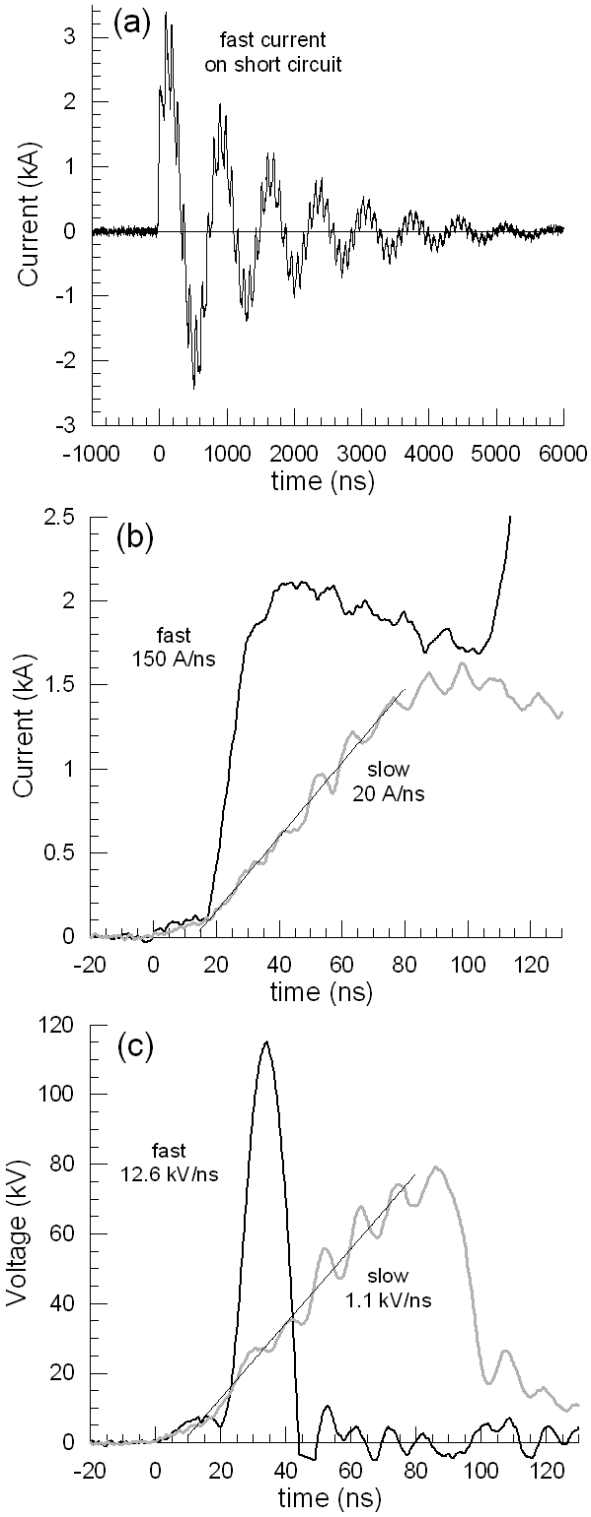

Fig. 3 Long time-scale waveform of the current on a short circuit (a); short time scale waveform of the fast and slow current on a short circuit (b); short time-scale waveform of the fast and slow voltage on open circuit (c).

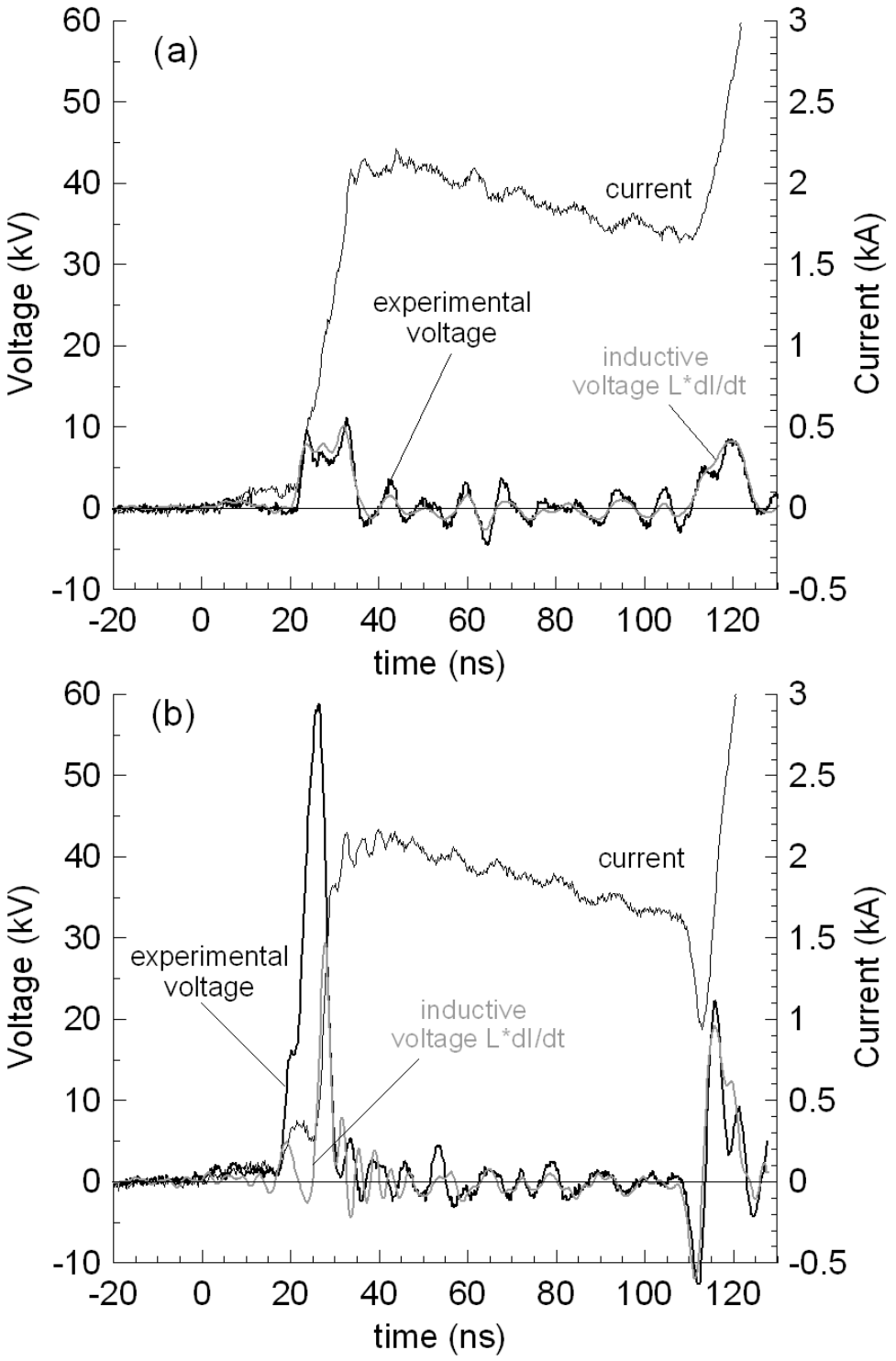

Fig. 4 Short-circuit waveforms for current, voltage and inductive voltage for Lo=50 nH (a). Exploding wires waveforms for current, voltage and inductive voltage for Lo= 50nH (b).

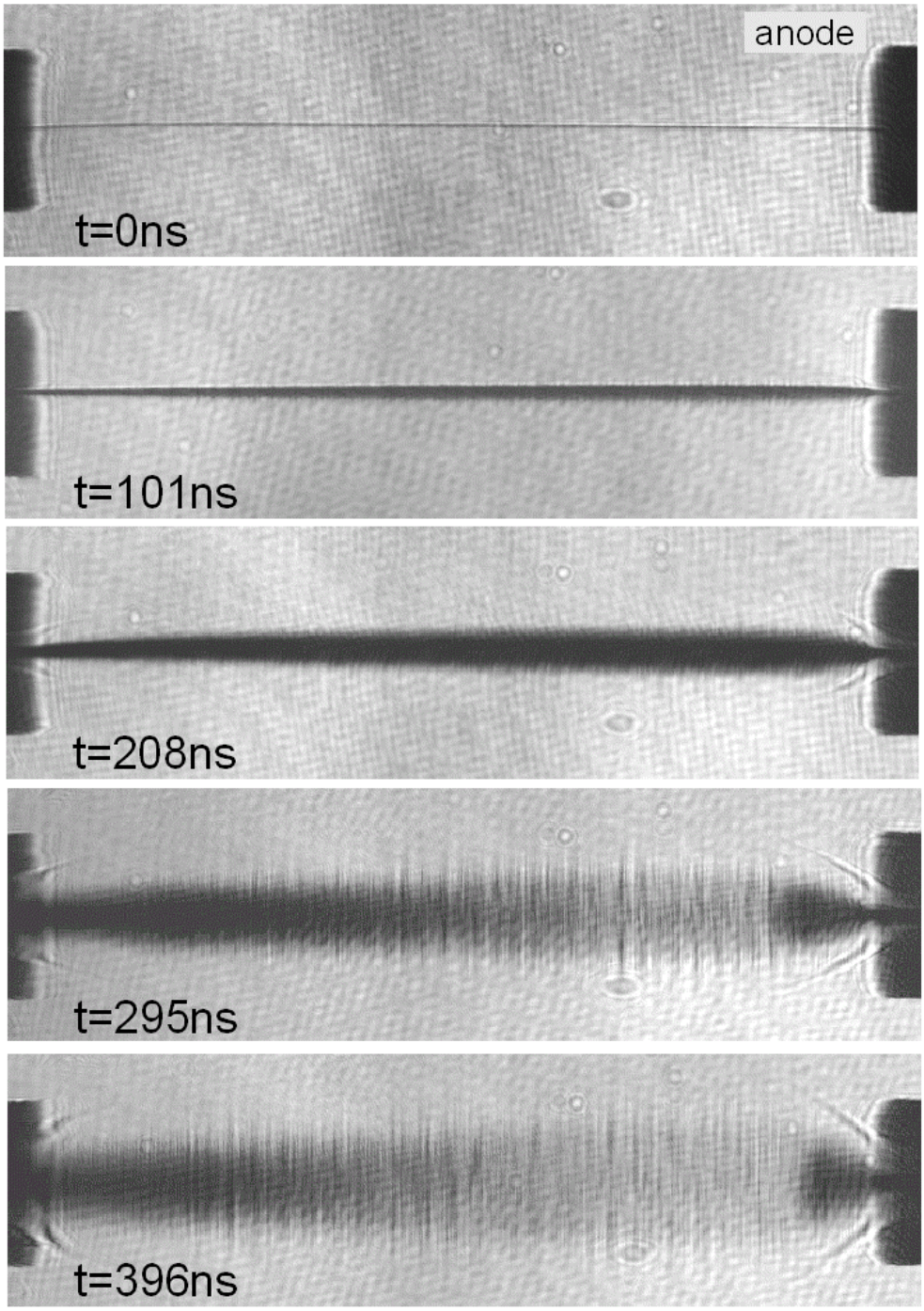

Fig. 5 Set of laser shadowgrams of slow exploding Al wires (20.3 μm diameter and 2 cm length) at different times.

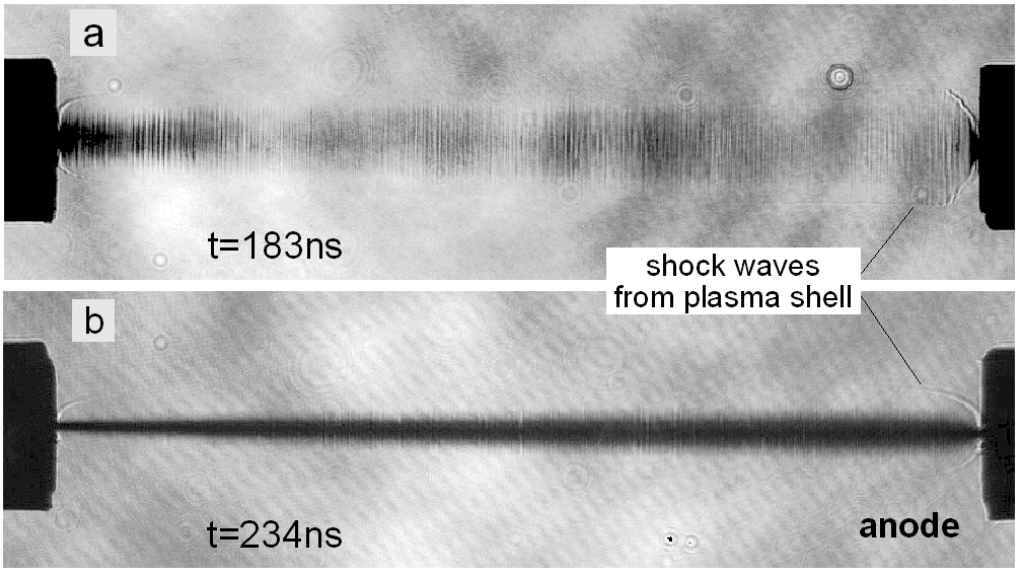

Fig. 6 Shadowgrams of the fast (a) and slow (b) explosion of 16.2 μm diameter and 2 cm long Al wires.

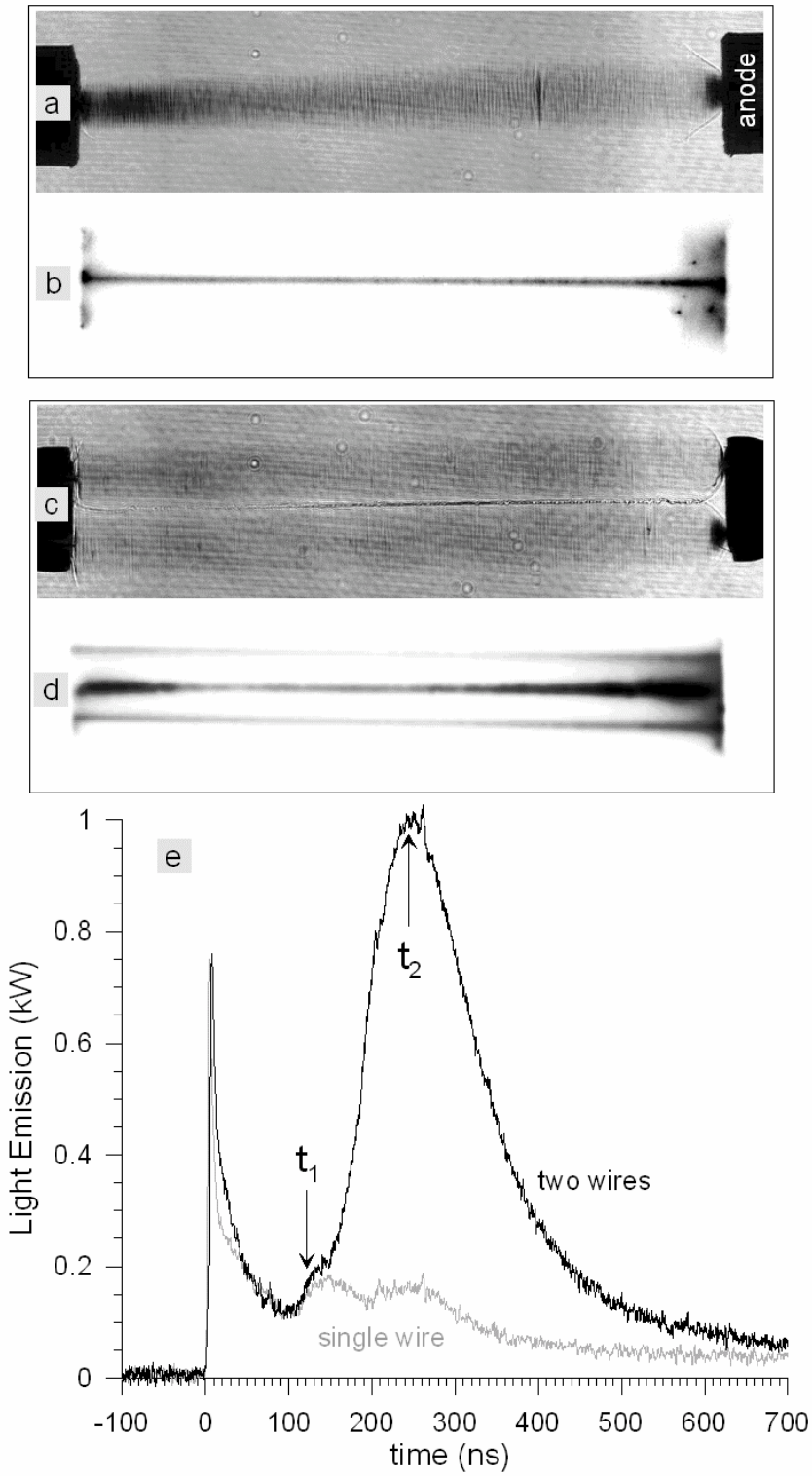

Fig. 7 Shadowgram (a) and open-shutter (b) images of single fast exploding 20.3 μm Al wires. Shadowgram (c) and open-shutter (d) images of two parallel fast exploding 20.3 μm Al wires (2 mm distance between wires). (e): Evolution of the light emission for single (a,b) and two parallel (c,d) wires.

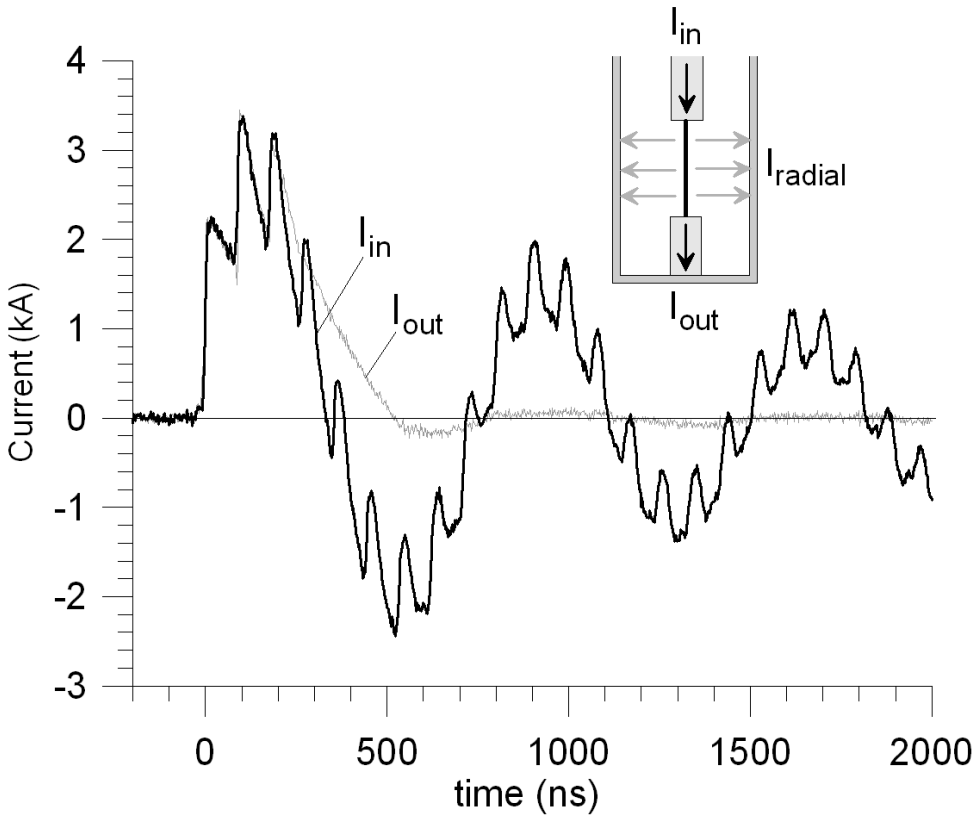

Fig. 8 Evolution of the upstream and downstream current for fast exploding 25.4 μm Al wire.

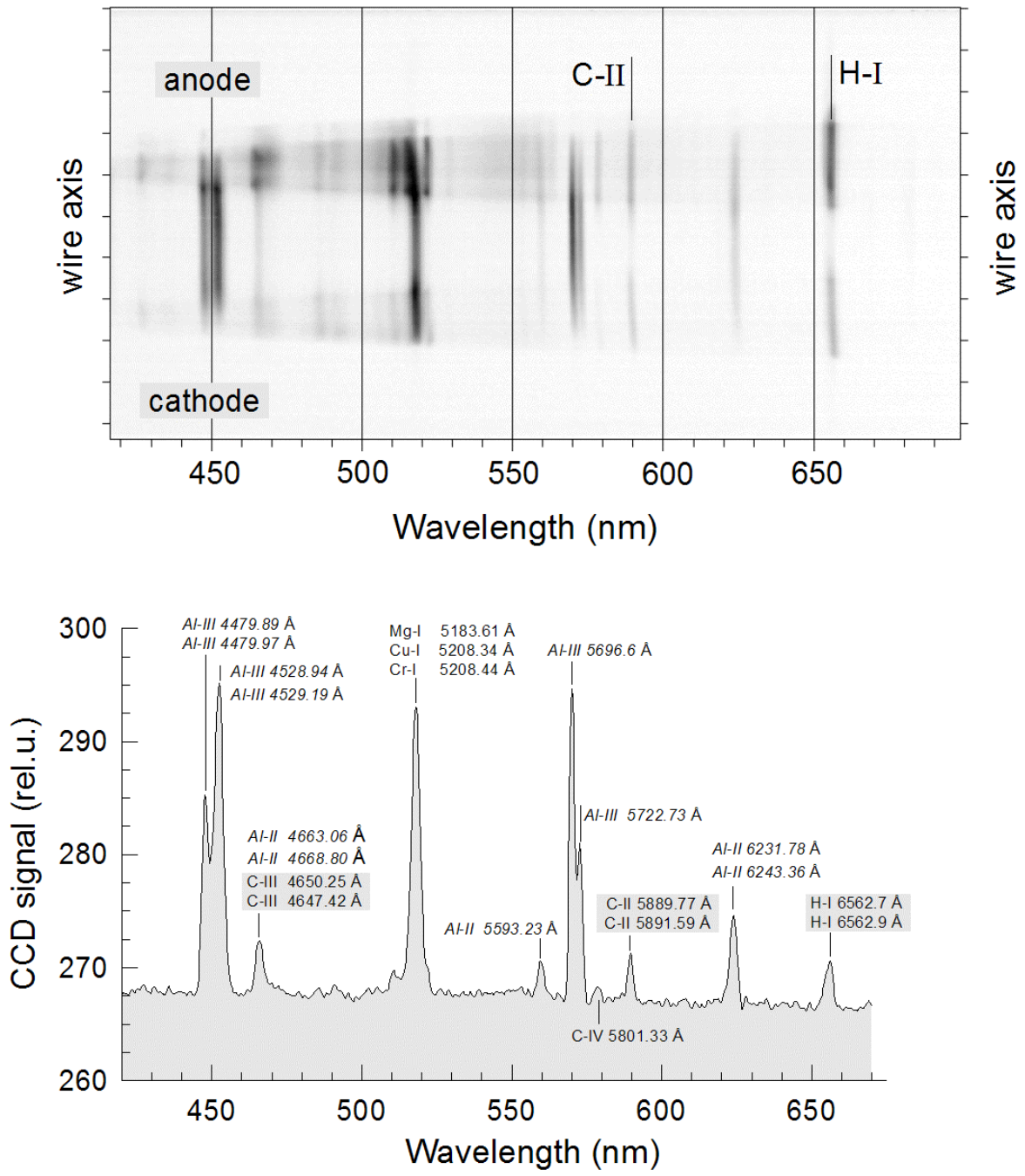

Fig. 9 The time-integrated optical spectra of the fast exploding 10 μm Al wire.

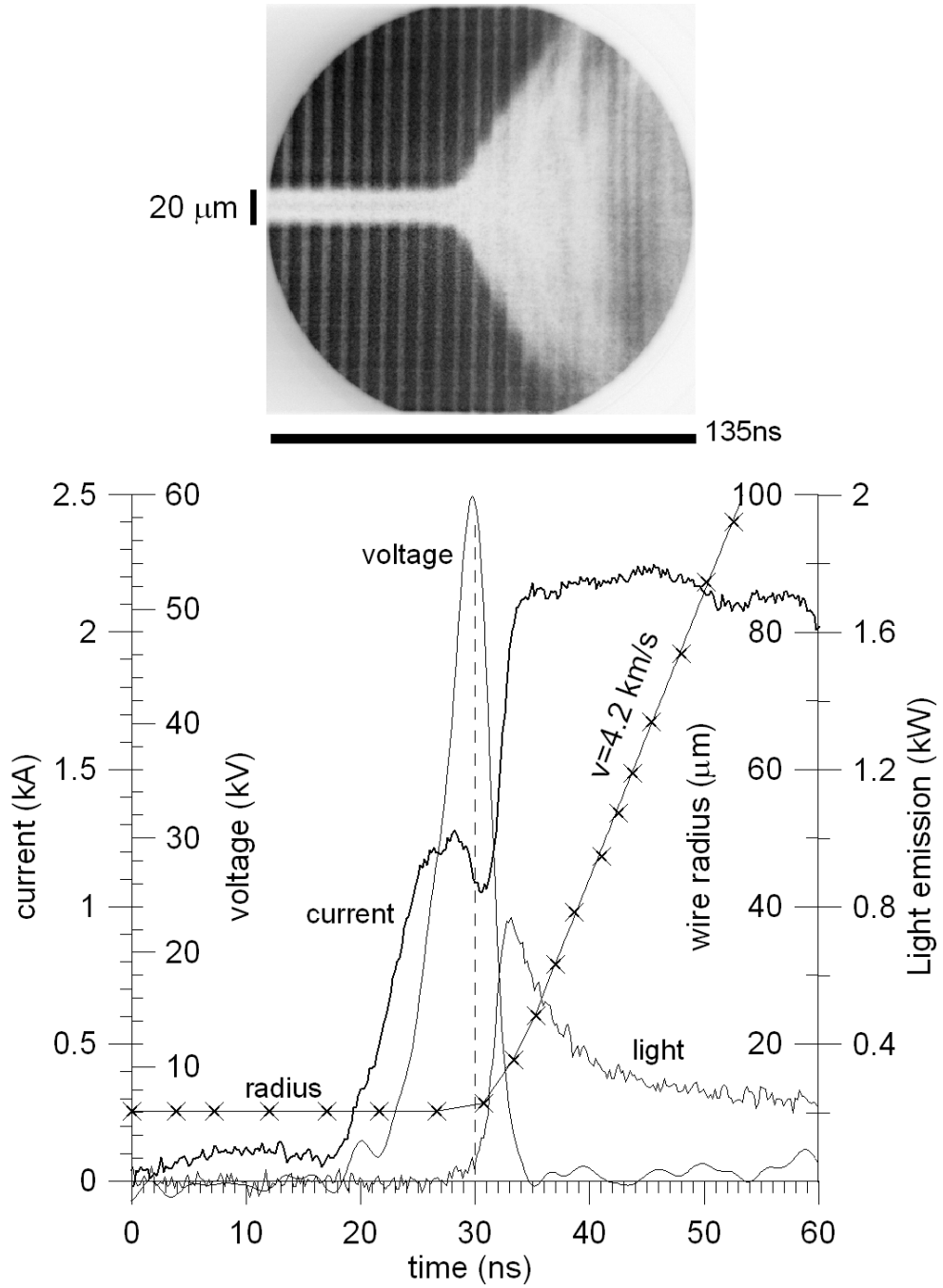

Fig. 10 Streak shadowgram image with 905 nm laser backlighter of the fast exploding 20.3 μm Al wire and appropriate waveforms of the current, voltage, light emission and wire radius. Light emission and wire expansion starts in a moment of the surface breakdown.

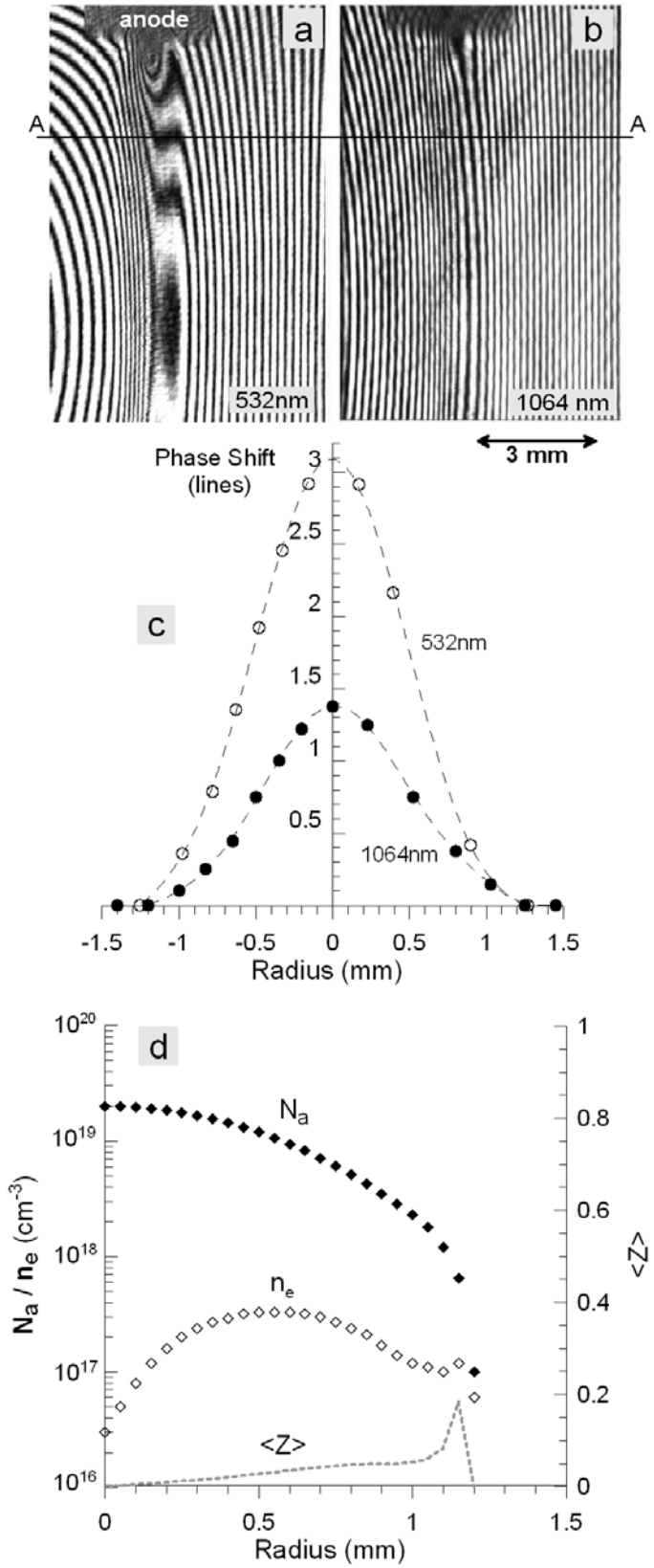

Fig. 11 Two-wavelength interferograms of fast exploding 25.4 μm Al wire (a,b) at 167 ns. Interference phase shift in cross-section A-A (c). Radial distribution N_a, n_e and Z for cross-section A-A (d).

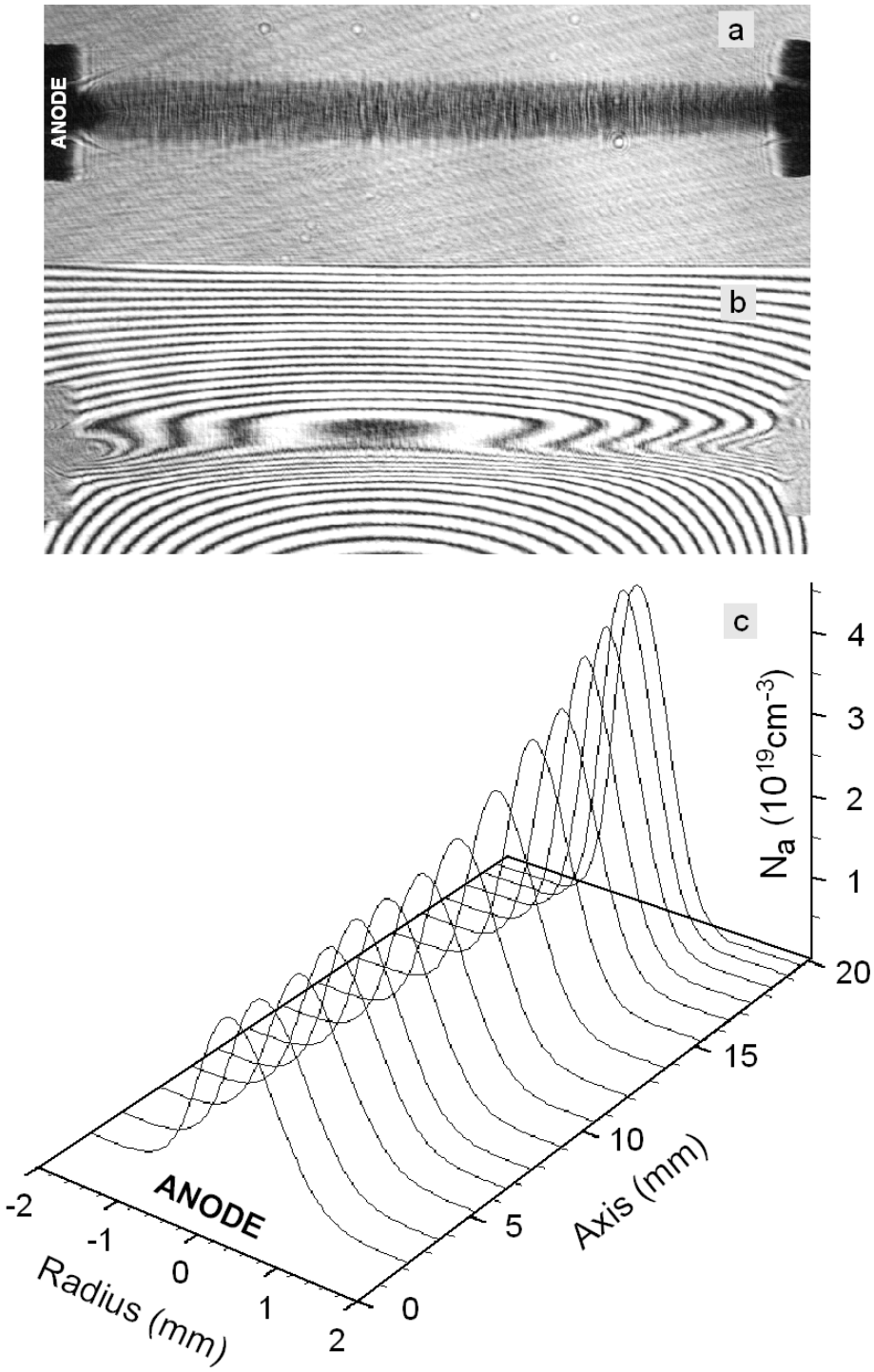

Fig. 12 Shadowgram (a) and interferogram (b) of 25.4 μm in diameter and 2 cm length Al wire at 196 ns after voltage maximum. Probing wavelength is 532 nm. 2D distribution of the atomic density (c) recovered using Abel inversion procedure.

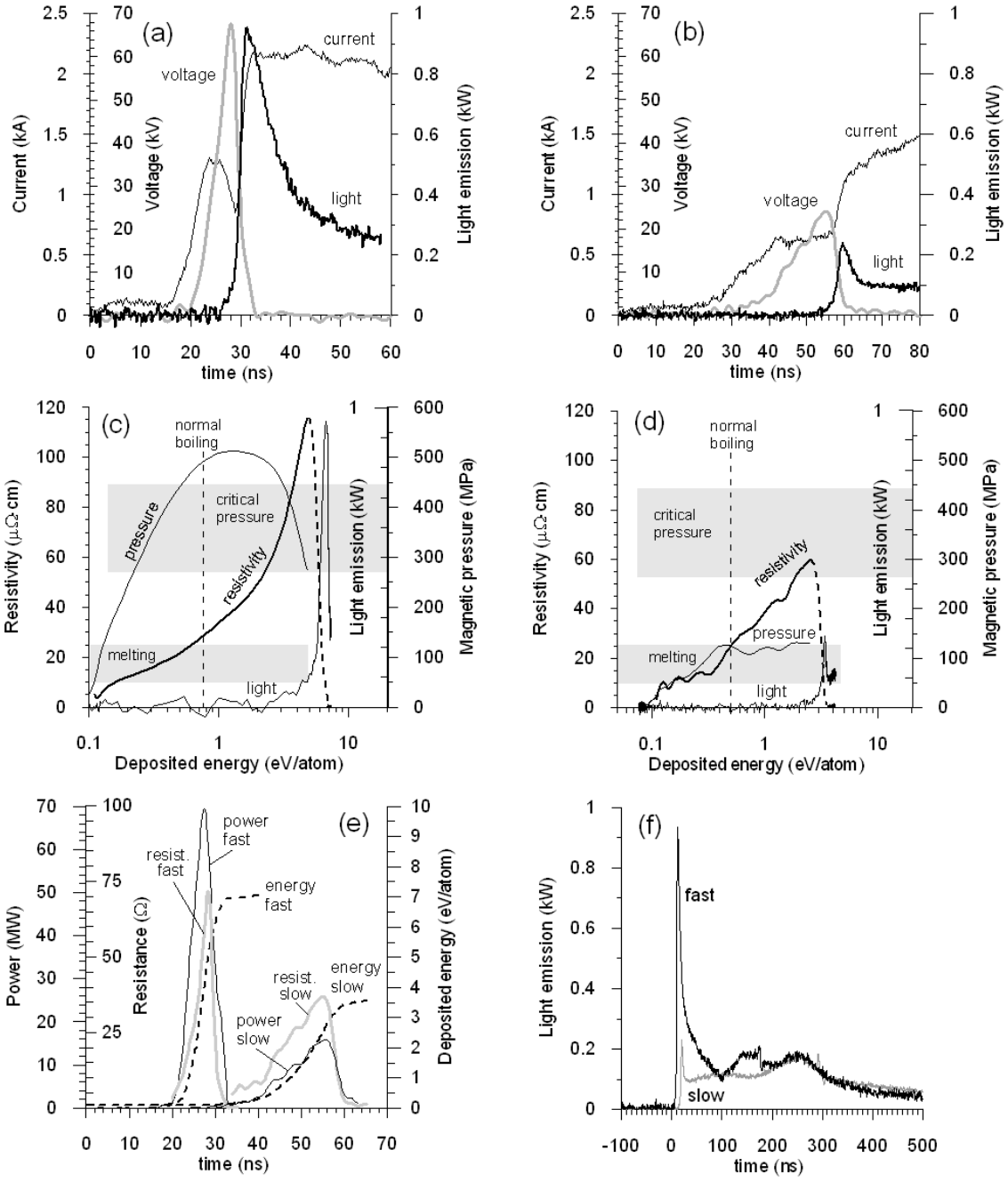

Fig. 13 Typical waveforms of current, voltage and light emission for fast (a) and slow (b) exploding 20.3 μm Al wires. Recovered distributions of the wire resistivity, magnetic field pressure and light emission vs. deposited energy for fast (c) and slow (d) explosions. Evolution of the electrical power and deposited energy for fast and slow explosions (e). Long time scale evolution of the light emission for fast and slow explosions (f).

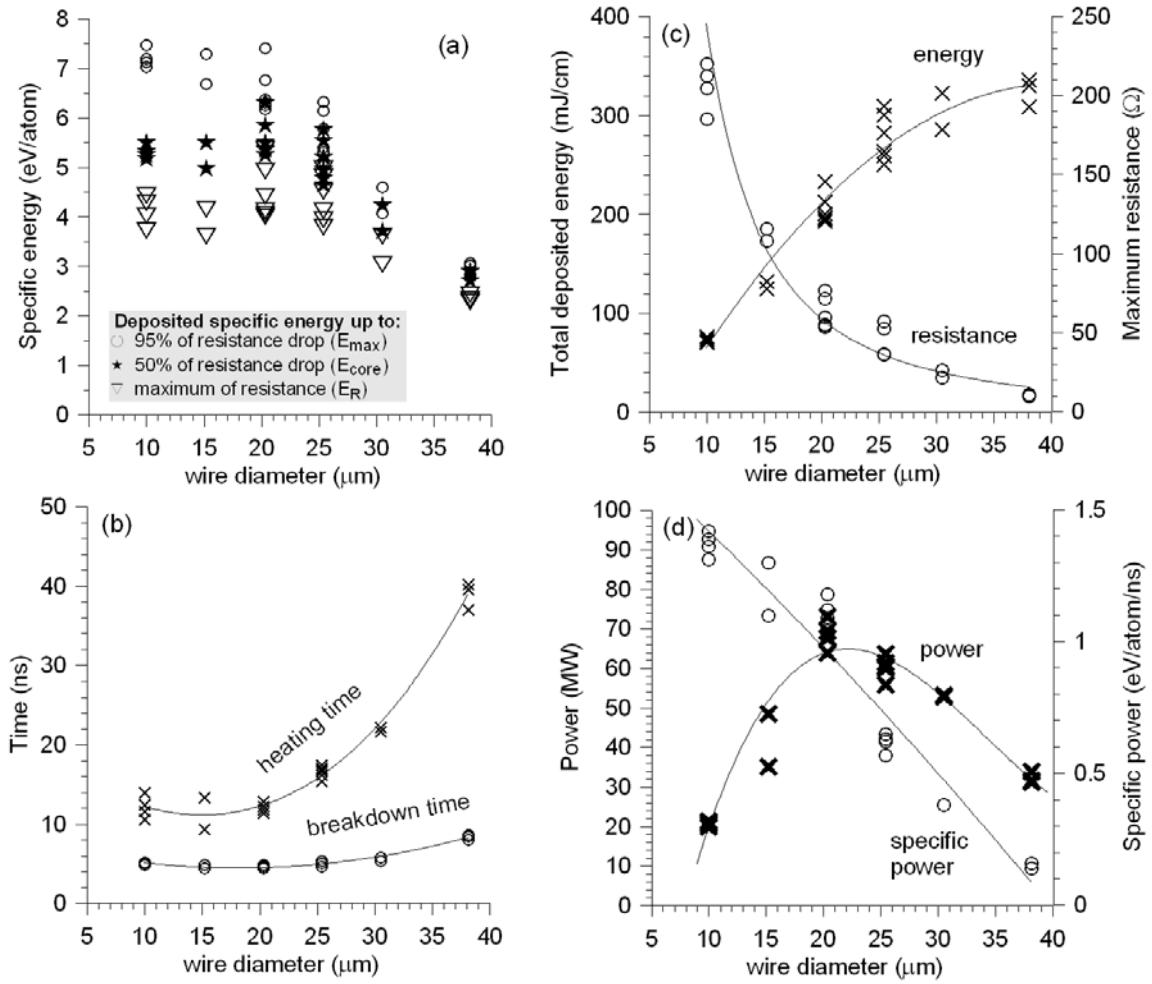

Fig. 14 Specific energy deposition vs. wire diameter (a). The time of wire heating and time of breakdown vs. wire diameter (b). Total deposited energy and wire maximum resistance vs. wire diameter (c). Electrical power and specific electrical power vs. wire diameter. All plots for fast explosion mode.

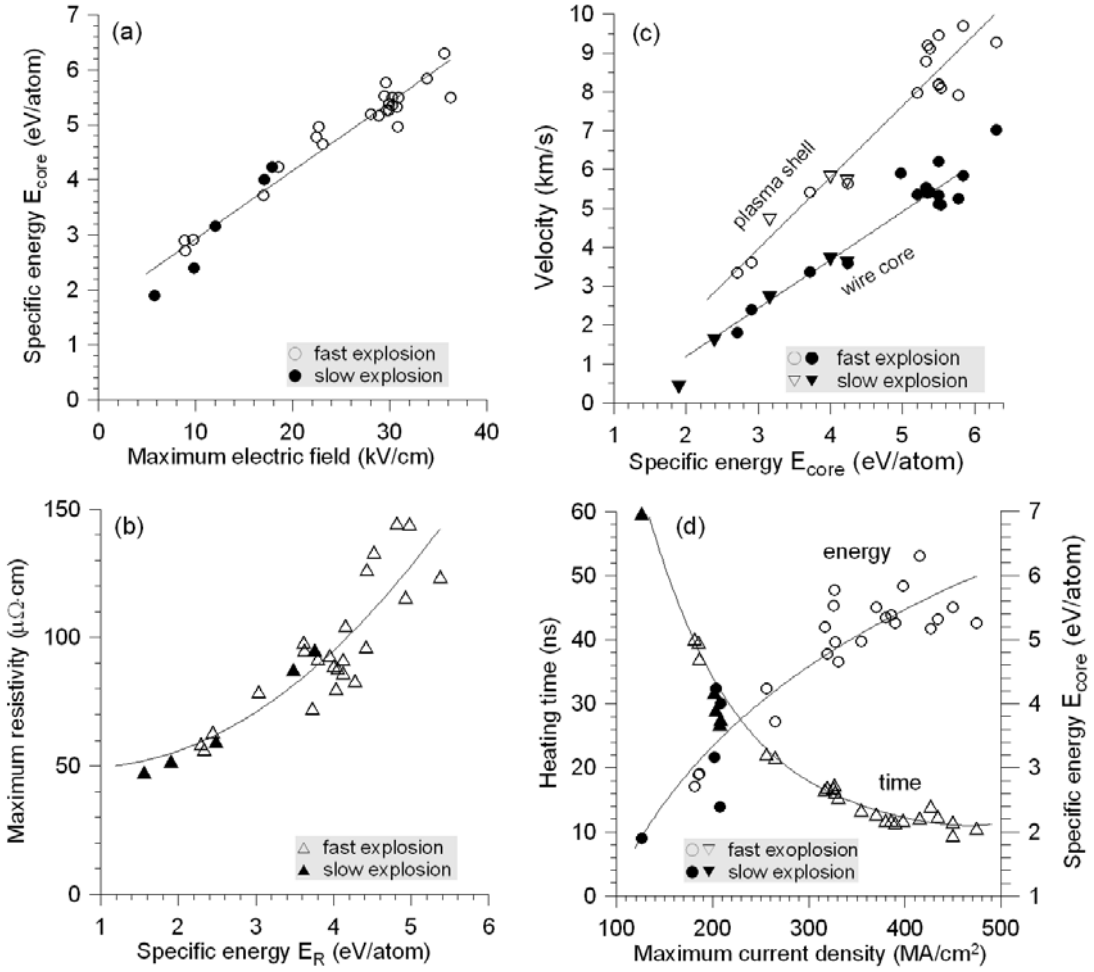

Fig. 15 Dependence of specific energy deposited into wire core vs. maximum value of electric field (a). Maximum wire resistivity vs. of deposited energy (b). Velocity of extending plasma shell and wire core vs. of deposited specific energy (c). Dependence of heating time and deposited specific energy vs. maximum current density (d).

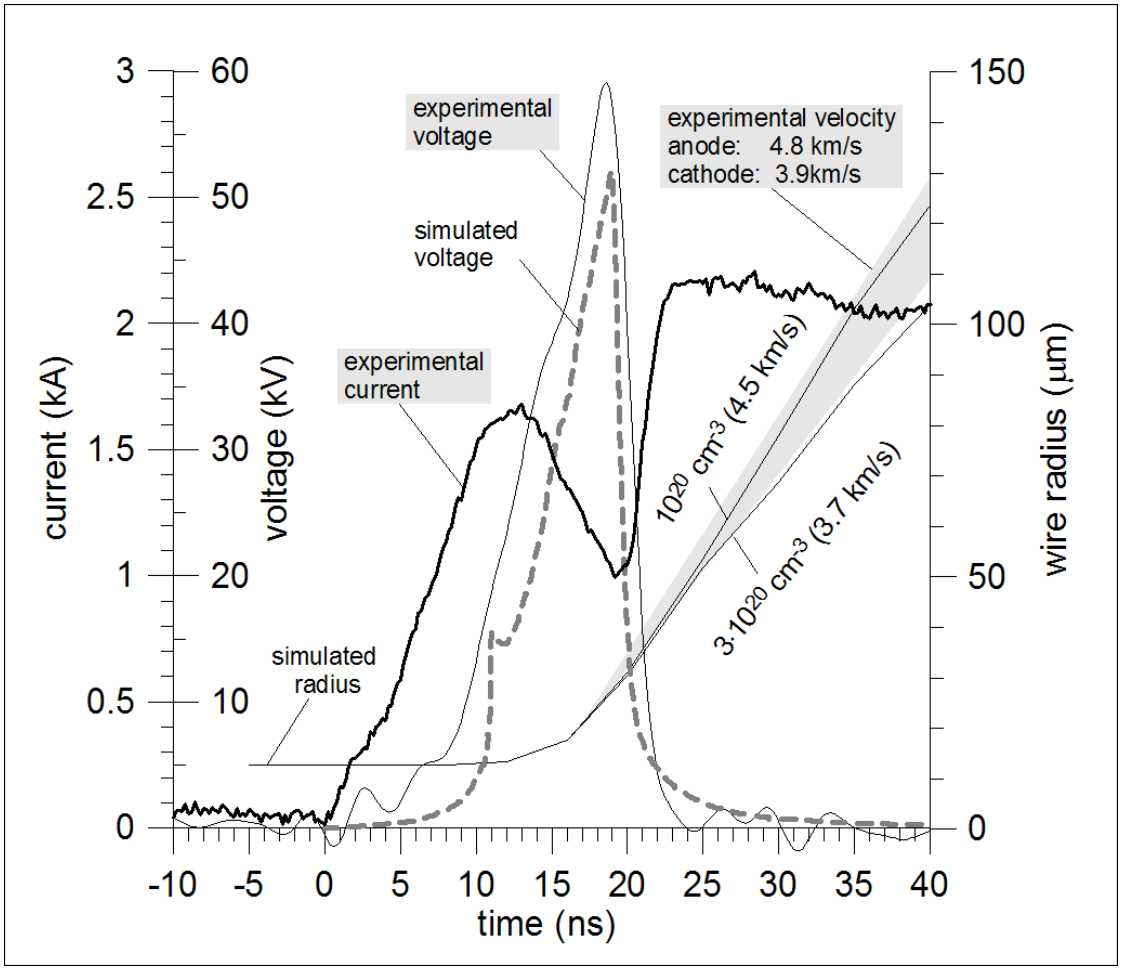

Fig. 16 Waveforms for current, voltage taken from experiment and simulated voltage (dash line), and wire radius (o) for fast exploding 25.4 μm Al wire. Gray triangle shows velocity of the extension of the wire core under anode and cathode.

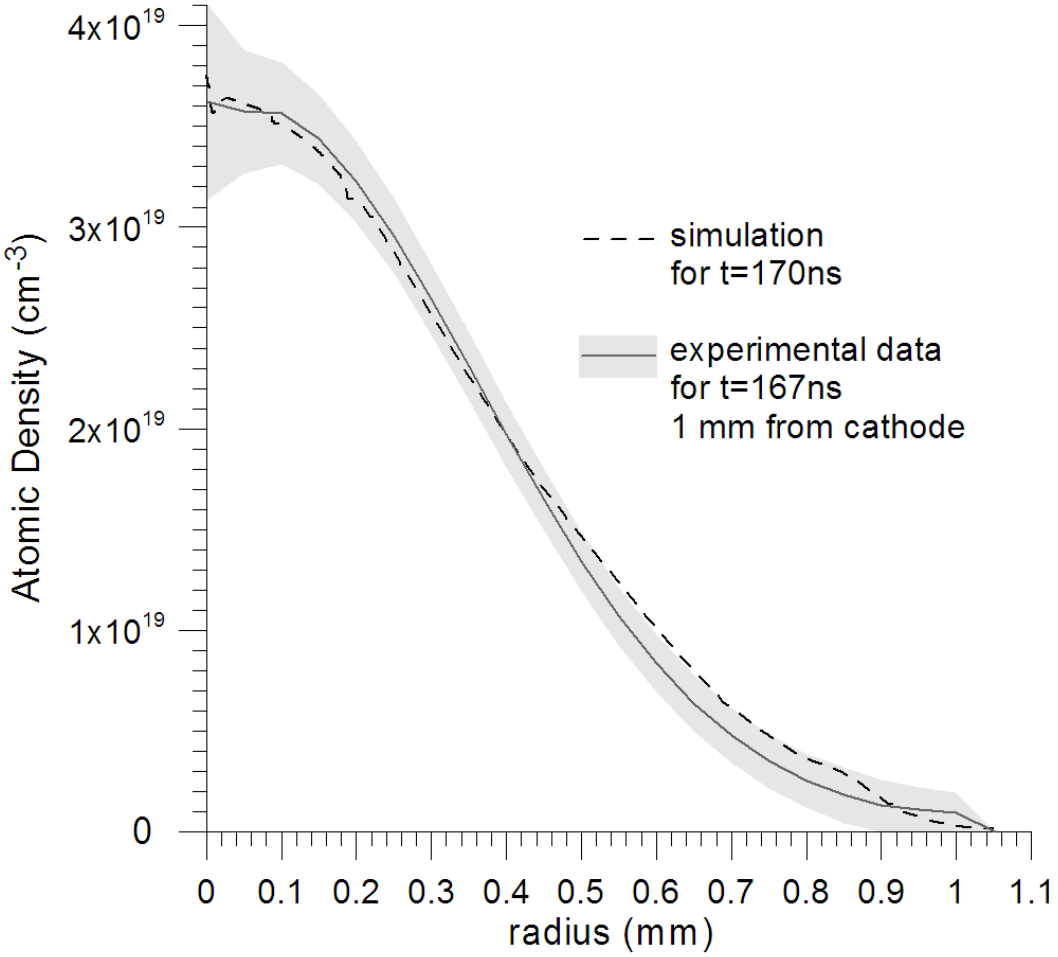

Fig. 17 Experimental and simulated radial distributions of the atomic density for 170 ns after voltage maximum.

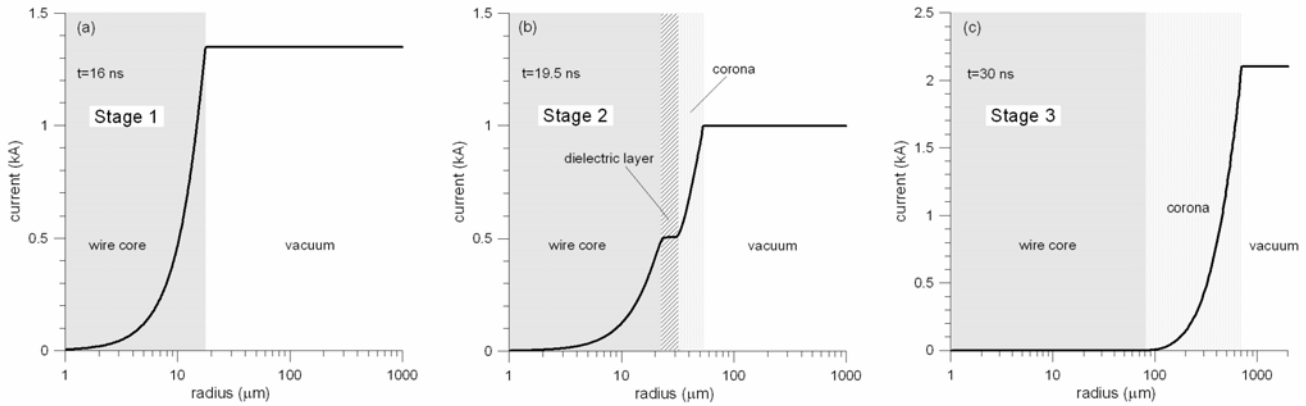

Fig. 18 Three basic stages of current distribution in fast exploding aluminum wire: **Stage 1**- current flow through the wire core (a); **Stage 2**- current switching from core to corona (b); **Stage 3**- current flow through the corona (c).

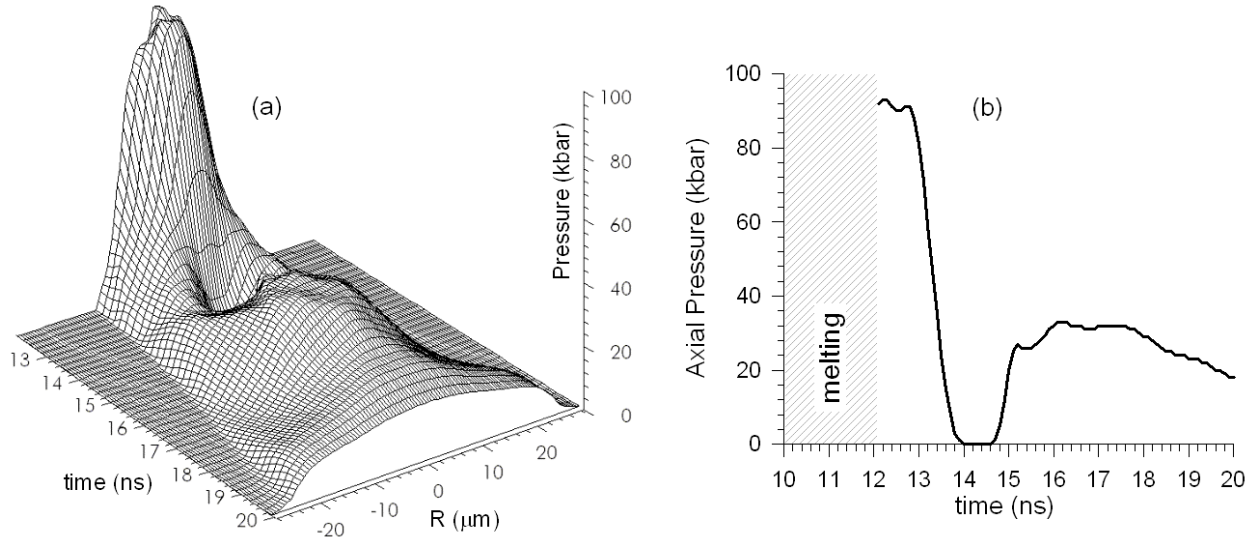

Fig. 19 Time and space-dependence of post-melt hydrodynamic pressure (a), time-dependence of axial pressure (b).

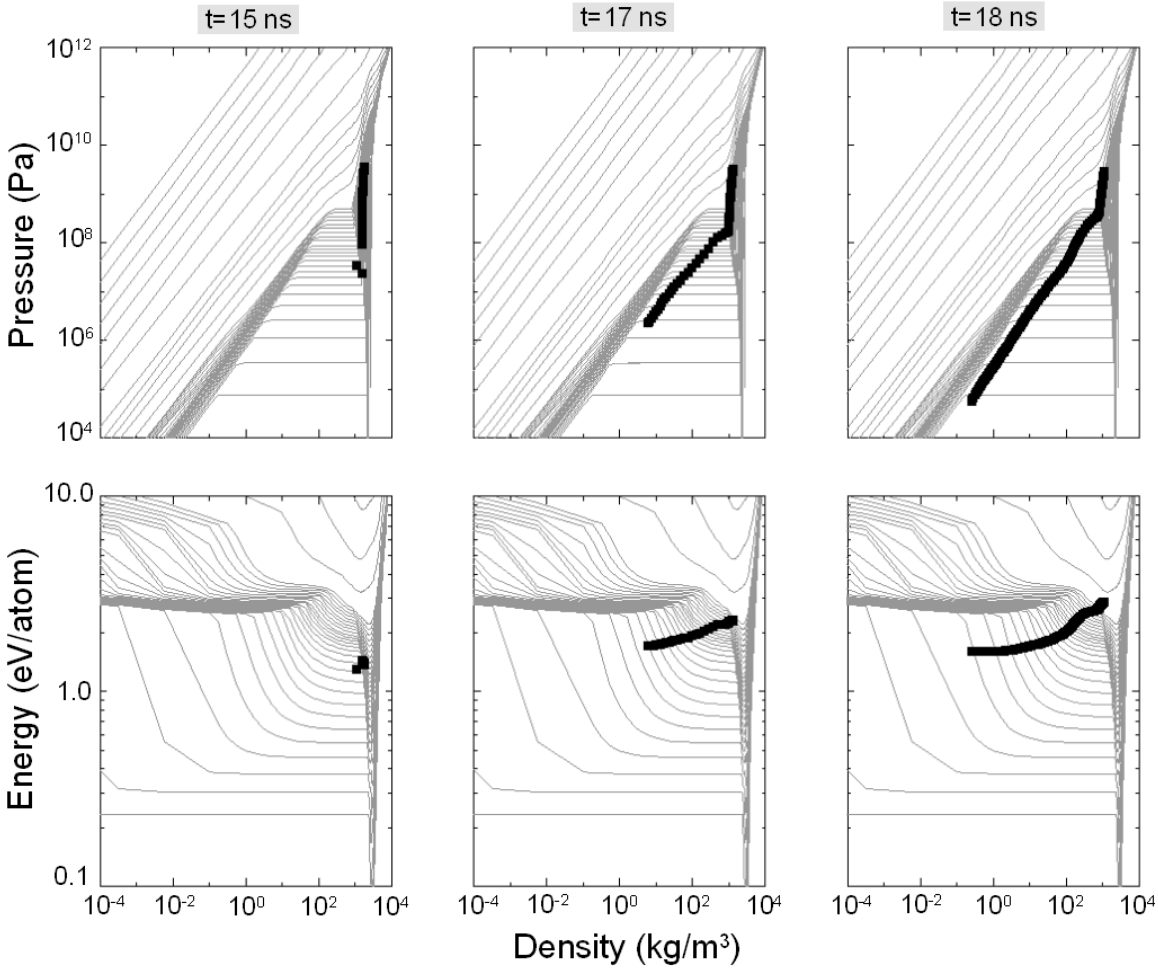

Fig. 20 Wire phase portraits at 15, 17, and 18 ns: (top) Pressure-density plane, (bottom) Specific energy-density plane.

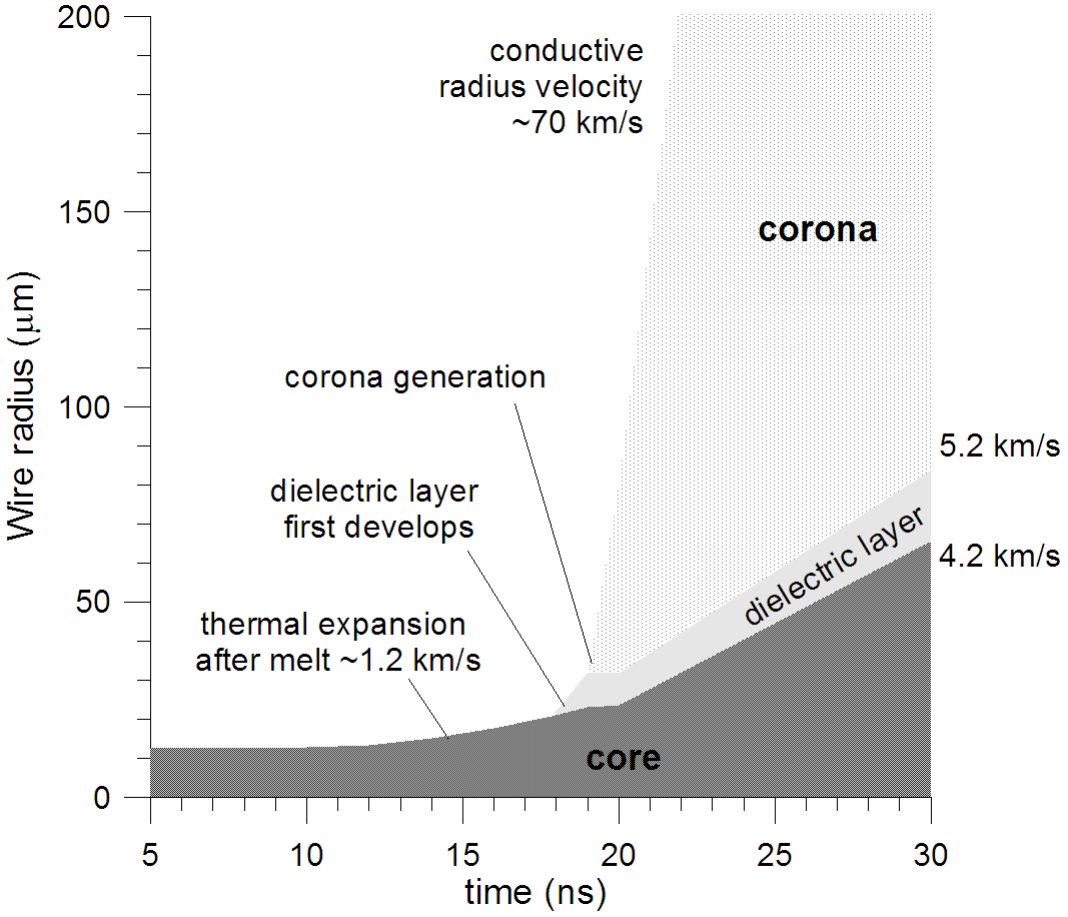

Fig. 21 Time-dependent conductive-radius and material-radius velocities obtained from enclosed current snapshots.

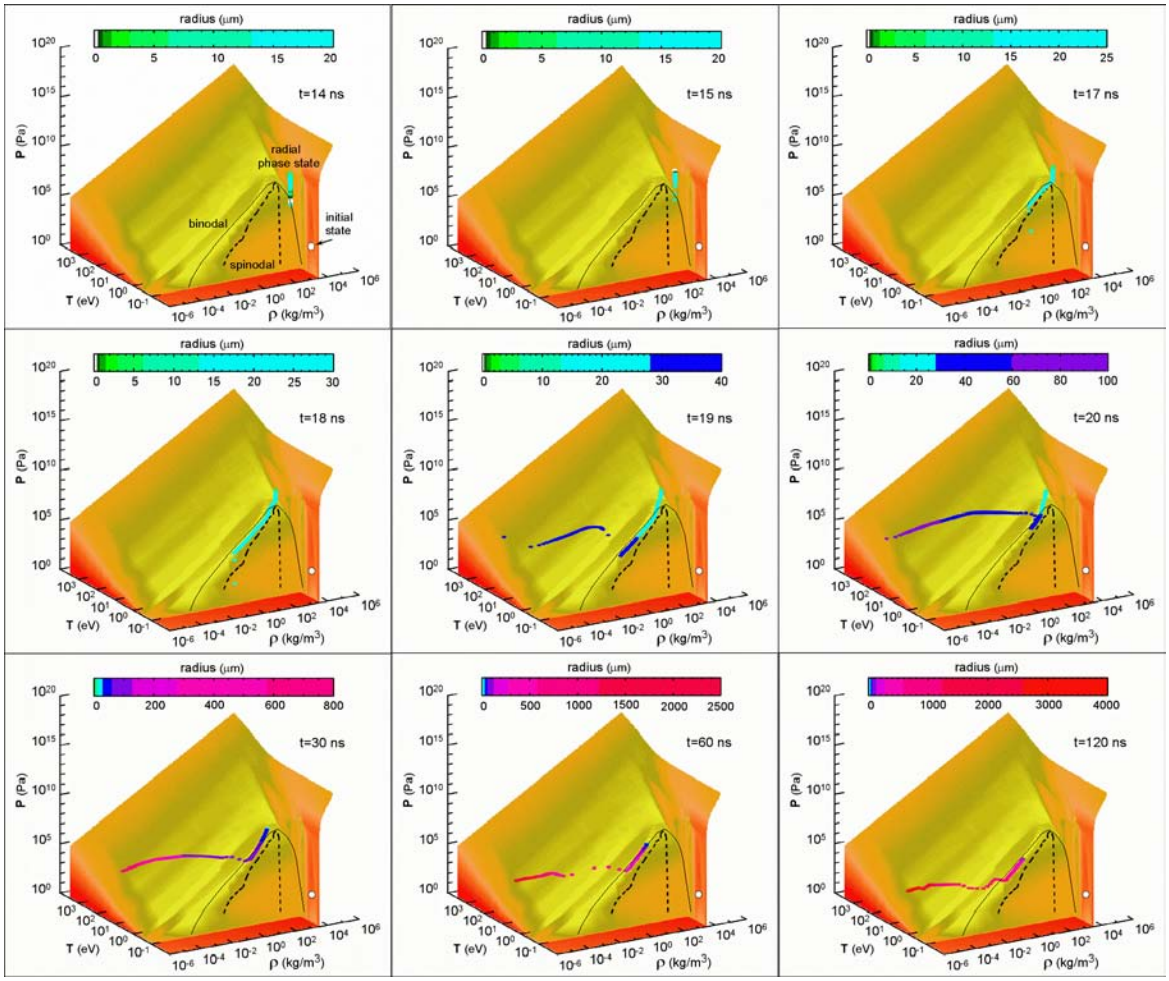

Fig. 22 Wire phase portraits on the EOS pressure surface at t = 14, 15, 17, 18, 19, 20, 30, 60, and 120 ns.

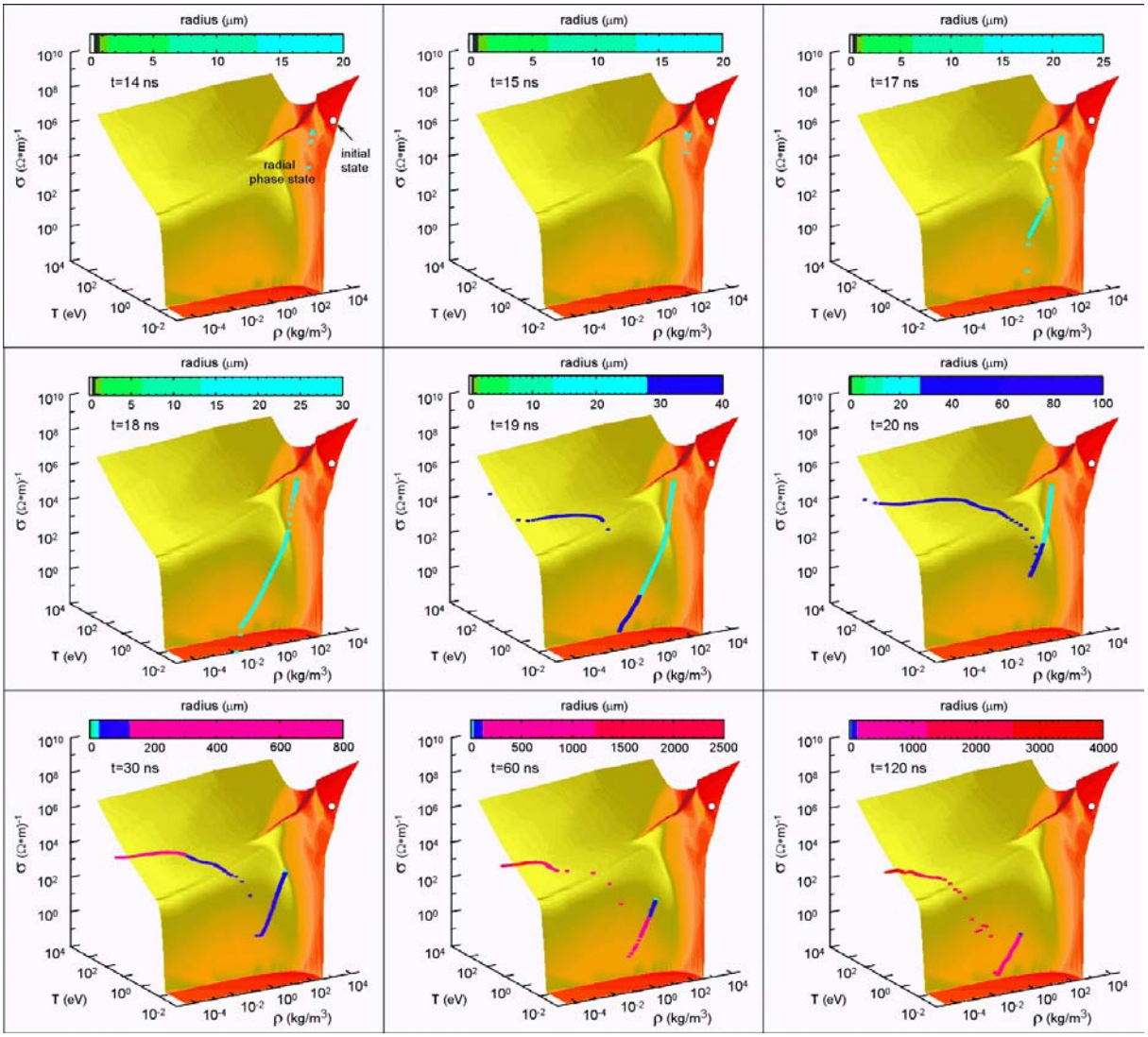

Fig. 23 Wire phase portraits on the conductivity surface at t = 14, 15, 17, 18, 19, 20, 30, 60, and 120 ns.

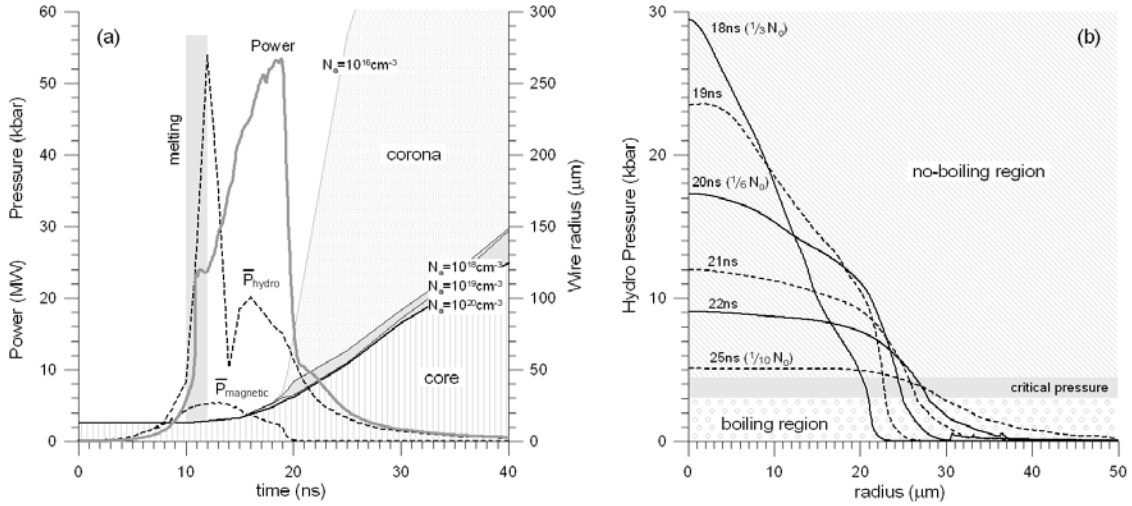

Fig. 24 Evolution of the electrical power, isolines of atomic density, average hydro and magnetic pressures (a). Radial profiles of hydro pressure during voltage collapse time (b).

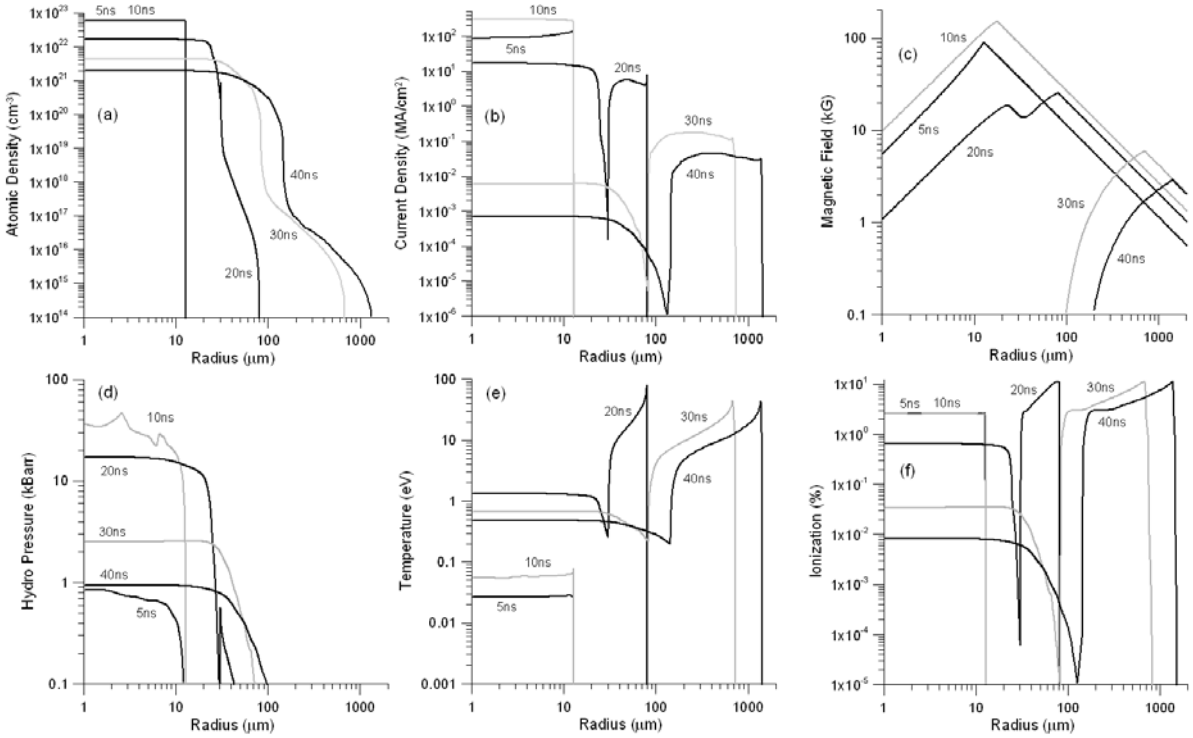

Fig. 25 Simulation radial profiles at different times (5, 10, 20, 30, 40 ns) for atomic density (a), current density (b), magnetic field (c), hydro-pressure (d), temperature (e), and ionization (f).

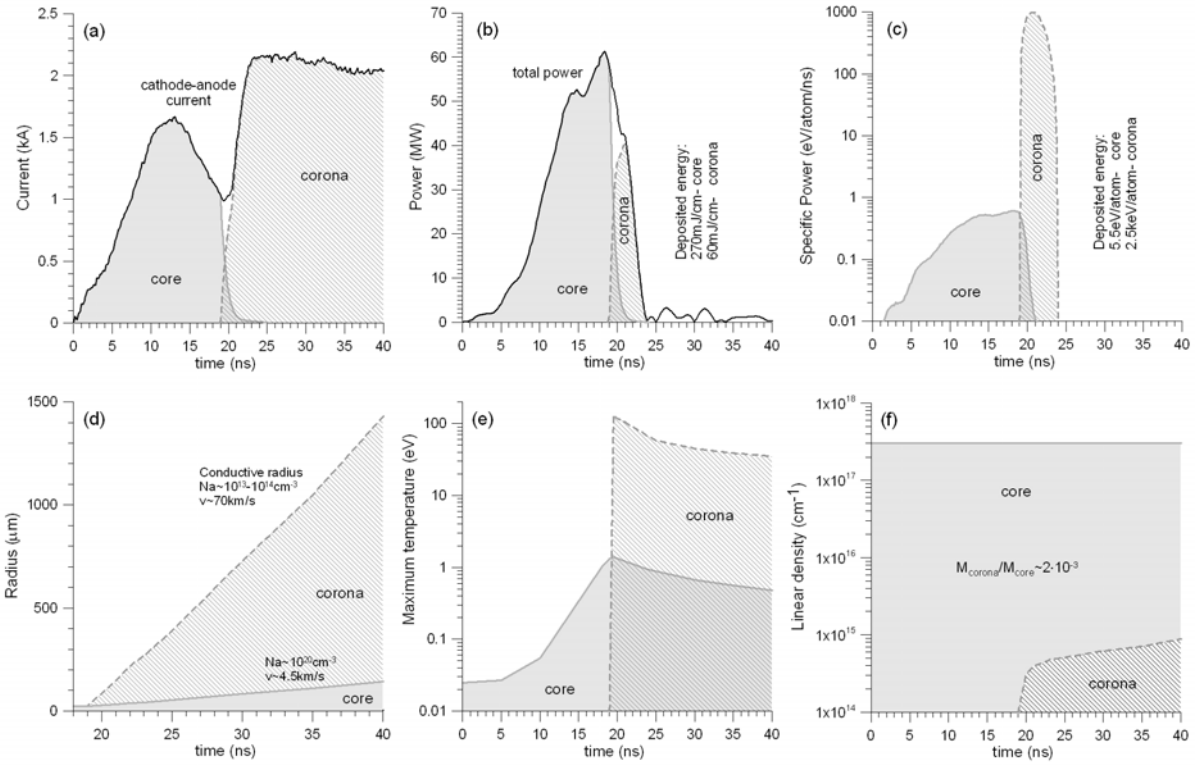

Fig. 26 Results of simulation summarizing core-corona evolution: current splitting between wire core and corona (a); evolution of the electrical power (b) and specific power (c) for wire core and corona; evolution of the radius for wire core and corona (d); evolution of the maximum temperature for wire core and corona (e); evolution of the linear density for wire core and corona (f).

SAND2004-2869
Printed June 2004